# Quasi 12 h inertia-gravity waves in the lower mesosphere observed by the PANSY radar at Syowa Station (39.6°E, 69.0°S)

Ryosuke Shibuya[1], Kaoru Sato[1], Masaki Tsutsumi[2,3],

Toru Sato[4], Yoshihiro Tomikawa[2,3],

Koji Nishimura[2,3] and Masashi Kohma[1]

[1] *Department of Earth and Planetary Science, The University of Tokyo, Tokyo, Japan*

[2] *National Institute of Polar Research, Tachikawa, Japan*

[3] *The Graduate University for Advanced Studies (SOKENDAI), Tokyo, Japan*

[4] *Department of Communications and Computer Engineering, Kyoto University, Japan*

*Corresponding to,* Ryosuke Shibuya, The University of Tokyo, 7-3-1 Hongo, Bunkyo-ku,

Tokyo 113-0033, Japan. E-mail: shibuya@eps.s.u-tokyo.ac.jp.

**Abstract**

The first observations made by a complete PANSY radar system (Program of the Antarctic Syowa MST/IS Radar) installed at Syowa Station (39.6°E, 69.0°S) were successfully performed from March 16 – 24, 2015. Over this period, quasi-half-day period (12 h) disturbances in the lower mesosphere at heights of 70 km to 80 km were observed. Estimated vertical wavelengths, wave periods and vertical phase velocities of the disturbances were approximately 13.7 km, 12.3 h and −0.3 m s$^{-1}$, respectively. Under the working hypothesis that such disturbances are attributable to inertia-gravity waves, wave parameters are estimated using a hodograph analysis. The estimated horizontal wavelengths are longer than 1100 km, and the wavenumber vectors tend to point northeastward or southwestward. Using the non-hydrostatic numerical model with a model top of 87 km, quasi 12 h disturbances in the mesosphere were successfully simulated. We show that quasi 12 h disturbances are due to wave-like disturbances with horizontal wavelengths longer than 1400 km and are not due to semi-diurnal migrating tides. Wave parameters, such as horizontal wavelengths, vertical wavelengths and wave periods, simulated by the model agree well with those estimated by the PANSY radar observations under the above-mentioned assumption. The parameters of the simulated waves are consistent with the dispersion relationship of the inertia-gravity wave. These results indicate that the quasi 12 h disturbances observed by the PANSY radar are attributable to large-scale inertia-gravity waves. By examining a residual of the nonlinear balance equation, it is inferred that the inertia-gravity waves are likely generated by the spontaneous radiation mechanism of two different jet streams. One is the mid-latitude tropospheric jet around the tropopause while the other is the polar night jet. Large vertical fluxes of zonal and meridional momentum associated with large-scale inertia-gravity waves are distributed across a slanted region from the mid-latitude lower stratosphere to the polar mesosphere in the meridional cross-section. Moreover, the vertical flux of the zonal momentum has a strong negative peak in the mesosphere, suggesting that some large-scale inertia-gravity

1   waves originate in the upper stratosphere. [335words]

3   Keywords: Gravity wave, polar region, mesosphere, the PANSY radar

## 1.  Introduction

6       Gravity waves are atmospheric waves with a restoring force of buoyancy that can transport

7   momentum upward from the troposphere to the middle atmosphere (e.g., Fritts and Alexander

8   2003). Momentum deposition by gravity waves in the mesosphere is a major driving force for

9   the summer to winter pole material circulation in the mesosphere (e.g., Plumb 2002). Adiabatic

10  heating/cooling associated with vertical flow branches of the circulation maintain the thermal

11  structure, which is considerably different from the radiative equilibrium state. Gravity waves

12  also play an essential role in driving the quasi-biennial oscillation (QBO) and semi-annual

13  oscillation in the equatorial stratosphere (Sato and Dunkerton 1997; Haynes 1998; Baldwin et

14  al., 2003). In addition, it has been shown that gravity wave forcing is essential to the summer

15  hemispheric low-latitude part of winter stratospheric circulation (Okamoto et al., 2011).

16      Many observational studies have closely examined characteristics of gravity waves in the

17  troposphere, stratosphere and mesosphere (e.g., Sato 1994; Sato and Yamada, 1994; Pavelin et

18  al., 2001; Lane et al., 2004; Nastrom and Eaton 2006; Vaughan and Worthington, 2007;

19  Nakamura et al., 1993; Li et al., 2007; Lu et al., 2009; Nicolls et al., 2010; Chen et al., 2013).

20  It is well known that gravity waves have wide spectral ranges of horizontal wavelength from

21  several kilometers to several thousand kilometers and of observed period from several minutes

22  to several hours. Recently, several numerical models directly resolve large parts of gravity

23  wave spectra (the KANTO model, Watanabe et al., 2008; WACCM, Liu et al., 2014; KMCM,

24  Becker, 2009). However, due to their short horizontal wavelengths, many climate models

25  utilize parameterization methods to calculate momentum deposition by unresolved gravity

26  waves (e.g., McFarlane 1987; Scinocca 2003; Richter et al., 2009). As parameterization

methods involve several tuning parameters related to characteristics of gravity waves, observational constraints on tuning parameters are inevitably required (e.g., Alexander et al. 2010).

Geller et al. (2013) showed that parameterized gravity waves in climate models are not realistic in several aspects in comparison to high-resolution observational data (satellites, isopycnic balloon observations and radiosondes) and gravity wave permitting general circulation models. In particular, they showed that gravity wave sources in the parameterization can be poorly specified in high latitude regions. Such an improper specification of gravity wave sources in southern high latitude regions is considered to lead several serious problems. One of these problems is the so-called cold-pole bias, present in the most climate models in the polar winter stratosphere (Eyring et al., 2010; McLandress et al. 2012). This bias is closely related to significant delays in the breakdown of the stratospheric polar vortex in the Antarctic (Stolarski et al., 2006). Gravity waves in the southern polar region modify formations of polar stratospheric clouds (PSCs), which can enhance ozone depletion in the polar lower stratosphere (Shibata et al., 2003; Watanabe et al. 2006; McDonald et al., 2009; Kohma and Sato, 2011). Moreover, Chu et al. (2011) reported that inertia-gravity waves in the polar mesosphere also affect the formation of polar mesospheric clouds (PMCs). Thus, observational studies of gravity waves around the southern high latitude region are quite important (e.g., Hertzog et al., 2008).

Recently, a Mesosphere-Stratosphere-Troposphere (MST) radar (or VHF clear-air Doppler radar) system was installed in the Antarctic. The system has completed continuous observations since April 30, 2012 at Syowa Station (69.0°S, 39.6°E) (the PANSY radar; Sato et al., 2014). The radar system provides vertical profiles of three-dimensional winds at high time and height resolutions. The PANSY radar system is a powerful tool for examining gravity waves in the high latitude region and many other scientific issues related to the polar

1    atmosphere.

2    One interesting phenomenon observed in the polar mesosphere is a large-amplitude wave-

3    like disturbance with near inertia-frequency (approximately 12 h) that many previous studies

4    have examined (e.g., Murphy et al., 2006; Akmaev et al., 2016). There are several explanations

5    for the existence of such oscillations; Fraser and Khan (1990) and Fisher et al. (2002) posited

6    that these oscillations are attributable to a semi-diurnal migrating tide. Waterscheid et al. (1986)

7    and Collins et al. (1992) attributed these oscillations to a "pseudo-tide" mechanism related to

8    gravity-wave momentum deposition modulated by a semi-diurnal migrating tide. Hagan and

9    Forbes (2003) investigated the atmospheric response to forcing by zonally asymmetric latent

10   heat release in the troposphere. Talaat and Mayr (2011) found that internal oscillations may be

11   caused by parameterized gravity waves in the model. Other studies (Hernandez et al., 1993;

12   Forbes et al., 1995, 1999; Fritts et al, 1998; Portnyagin et al. 1998; Yamashita et al., 2002; Wu

13   et al., 2003, Aso 2007, Murphy et al., 2009) suggest that these oscillations are due to semi-

14   diurnal non-migrating tides with zonal wavenumber $s = 1$ generated by nonlinear interactions

15   between $s = 1$ stationary planetary waves and semi-diurnal migrating tides. Mayr et al. (2005a,

16   b) emphasized the importance of gravity wave filtering effects on nonlinear interactions. Riggin

17   et al. (1999) showed that the zonal wavenumber of the 12 h wave is close to two in the winter

18   and is one in the summer based on radar observations conducted at McMurdo (77.8°S) and

19   Halley (75.8°S). Wu et al. (2002) suggested that $s = 1$ semi-diurnal non-migrating tides are

20   significant at latitudes of higher than 78° and that a mixture of semi-diurnal migrating tides and

21   $s = 1$ semi-diurnal non-migrating tides appears at between 68° and 78°.

22   The first successful observation with a complete system of the PANSY radar was

23   performed for March 16 – 24, 2015. In this study, we used this observational dataset. During

24   this observation period, strong wave-like disturbances with a wave period of about 12 h were

25   found in the lower mesosphere. Using PANSY radar data and a gravity wave resolving model,

generation and propagation mechanisms of such disturbances were examined. It is suggested

that wave-like disturbances with a wave period of about 12 h are attributable to large-scale

inertia-gravity waves with horizontal wavelengths of larger than 1100 km.

The present article is organized as follows. The methodology used is described in Section

2. Observational results are presented in Section 3. The results of the model simulations are

given and compared with radar observations in Section 4. Propagation characteristics and the

wave generation mechanism are also examined. A discussion is presented in Section 5, and

Section 6 summarizes the results and provides concluding remarks.

## 2.   Methodology
### 2.1. The PANSY radar observations

The PANSY (Program of the Antarctic Syowa MST/IS radar) radar system is the first

MST/IS radar system installed at Syowa Station (39.6°E, 69.0°S) for observing the Antarctic

atmosphere in a height region from 1.5 km to 500 km. It should be noted that an observation

gap exists at a height region from 30 km to 60 km, due to the lack of the atmospheric radar

backscattering in this height region (Sato et al., 2014). The PANSY radar system employs a

pulse-modulated monostatic Doppler radar system with an active phased mechanism consisting

of 1045 crossed-Yagi antennas. The PANSY radar system is designed to observe three-

dimensional winds at a high time resolution and vertical resolution along beam directions of

$\Delta t$ = ~1 min and $\Delta z$ = 150 m in the troposphere and lower stratosphere, respectively, and of

$\Delta t$ = ~1 min and $\Delta z$ = 600 m in the mesosphere. The accuracy of line-of-sight wind velocity

is about 0.1 m s$^{-1}$. As the target of MST radars is atmospheric turbulence, wind measurements

can be made under all weather conditions. Continuous observations have been made by the

PANSY radar through a partial system since April 30, 2012. The first observation with the

complete system of the PANSY radar observation was successfully performed for March 16 –

24, 2015. See Sato et al. (2014) for further information on the PANSY radar system and for a

1    list of future studies to be conducted based on this system. For the March 16 – 24, 2015 period,

2    strong polar mesosphere winter echoes, which likely resulted from the largest magnetic storm

3    event occurring during the solar cycle 24 ("St. Patrick's day storm", Kataoka et al., 2015;

4    Jacobsen and Andalsvik 2016; Cherniak and Zakharenkova 2016), were observed by the

5    PANSY radar system.

6        The PANSY radar data that we used are line-of-sight wind velocities of five vertical beams

7    tilted east, west, north and south at a zenith angle of $\theta$ =10°. Vertical wind components are

8    directly estimated from the vertical beam. Zonal (meridional) wind components are obtained

9    using a pair of line-of-sight velocities of the east and west beams (the north and south beams).

10   For example, line-of-sight velocities of the east and west beams, $V_{\pm\theta}$, are composed of zonal

11   and vertical components of the wind velocity vectors $(u_{\pm\theta}, w_{\pm\theta})$ in the targeted volume

12   ranges:

$$V_{\pm\theta} = \pm u_{\pm\theta} \sin\theta + w_{\pm\theta} \cos\theta.$$

13   By assuming that the wind field is homogeneous at each height, i.e., $u_{+\theta} = u_{-\theta} \equiv u$ and

14   $w_{+\theta} = w_{-\theta} \equiv w$, we can estimate zonal wind components as:

$$u = \frac{V_{+\theta} - V_{-\theta}}{2\sin\theta}.$$

15   The vertical flux of zonal momentum is directly estimated from variances of line-of-sight wind

16   fluctuations (Vincent and Reid, 1983):

$$\overline{V'^2_{\pm\theta}} = \overline{u'^2_{\pm\theta}} \sin^2\theta + \overline{w'^2_{\pm\theta}} \cos^2\theta \pm \overline{u'_{\pm\theta} w'_{\pm\theta}} \sin 2\theta$$

17   By assuming that the flux and variance fields are homogeneous ($\overline{u'^2_{+\theta}} = \overline{u'^2_{-\theta}} \equiv \overline{u'^2}$, $\overline{w'^2_{+\theta}} =$

18   $\overline{w'^2_{-\theta}} \equiv \overline{w'^2}$ and $\overline{u'_{+\theta} w'_{+\theta}} = \overline{u'_{-\theta} w'_{-\theta}} \equiv \overline{u'w'}$), we obtain:

$$\overline{u'w'} = \frac{\overline{V'^2_{+\theta}} - \overline{V'^2_{-\theta}}}{2\sin 2\theta}.$$

23   This assumption is less strict than that used for the *u* and *w* estimates. Thus, the method based

24   on MST radars provides quite accurate estimates of momentum fluxes. The meridional wind

25   component and the vertical flux of meridional momentum can be estimated in a similar manner.

1    Reid and Vincent (1987) examined horizontal wavelengths by using the cross correlation

2    techniques and the sensitivities of the estimation with several observational periods. In this

3    study, wave parameters are estimated by a hodograph analysis described in Section 3.

5    **2.2. Numerical setup for non-hydrostatic model simulation**

6         The simulation was performed using the Non-hydrostatic Icosahedral Atmospheric Model

7    (NICAM), which a global cloud resolving model (Satoh et al., 2008, Satoh et al., 2014). A non-

8    hydrostatic dynamical core of the NICAM was developed from icosahedral grids modified by

9    the spring dynamics method (Tomita et al., 2002). The NICAM is unique in its use of a flux-

10   form non-hydrostatic equation system that assures the conservation of total mass, momentum

11   and energy over the domain.

13   **2.2.1. Horizontal and vertical coordinate system**

14        Resolutions of horizontal icosahedral grids are represented by glevel-$n$ (grid division level

15   $n$). Glevel-0 denotes the original icosahedron. By dividing each triangle into four small

16   triangles recursively, one-higher resolution is obtained. The total number of grid points is $N_g =$

17   $10 \cdot 4^n + 2$ for glevel-$n$. The actual resolution corresponds to the square root of the averaged

18   control volume area, $\Delta x \equiv \sqrt{4\pi R_E^2 / N_g}$, where $R_E$ is the Earth's radius. A glevel-7 grid is

19   used in this study ($\Delta x \sim 56$ km).

20        Recently, Shibuya et al. (2016) developed a new grid configuration for quasi-uniform and

21   regionally fine meshes within a circular region with icosahedral grids using spring dynamics.

22   This method clusters grid points over the sphere into the circular region (the targeted region)

23   and realizes finer meshes than original icosahedral grids. By introducing sets of mathematical

24   constraints, it has been shown that the minimum resolution within the targeted region is

25   uniquely determined by the area of the targeted region alone. In this study, the targeted region

26   for a given glevel is a region south of 30°S centered at the South Pole. Figure 1a shows an

illustration of the stretched grid which is roughened up to glevel-3. Figure 1b shows a horizontal map of a normalized grid interval defined as $d(\lambda, \phi)/\Delta x$, where $d$ denotes grid intervals as a function of the longitude, $\lambda$, and the latitude, $\phi$. In this case, the horizontal resolution in the targeted region is roughly 36 km.

To simulate structures of disturbances from the stratosphere to the mesosphere, the vertical grid spacing is 400 m at heights from 2.4 km to 80 km. It should be noted that according to Watanabe et al. (2015), gravity wave momentum flux is not heavily dependent on model vertical spacing in the middle atmosphere when $\Delta z < 400$ m. The number of vertical grids is 217. To prevent unphysical waves reflection at the top of the boundary, a 7 km thick sponge layer is set above z = 80 km. The second-order Laplacian horizontal hyper-viscosity diffusion and Rayleigh damping for the vertical velocity are used for the sponge layer. An *e*-folding time of the $\nabla^2$ horizontal diffusion for the $2\Delta x$ wave at the top of the model is 4 s, and an *e*-folding time of the Rayleigh damping for the vertical velocity for the top of the model is 216 s. The diffusivity level gradually increases from the bottom to the top of the sponge layer. We confirm that little wave reflection near the sponge layer occurs under this setting (not shown).

**2.2.2. Initial condition and other physical schemes**

MERRA reanalysis data based on the Goddard Earth Observing System Data Analysis System, Version 5 (GEOS-5 DAS; Rienecker et al. 2011) is used as the initial condition. In the MERRA reanalysis data, the following two types of 3-D fields are provided: one set is produced through the corrector segment of the Incremental Analysis Update (IAU, Bloom et al., 1996) cycle (1.25° × 1.25° and 42 vertical levels whose top is 0.1 hPa) and the other pertains to fields resulting from Gridpoint Statistical Interpolation analyses (GSI analysis, e.g., Wu et al., 2002) on the native horizontal grid and on native model vertical levels (0.75° × 0.75° and 72 vertical levels whose top is 0.01 hPa). We use the former 3-D assimilated fields for 1000 hPa to 0.1 hPa and the latter 3-D analyzed fields for 0.1 hPa to 0.01 hPa for the initial condition of the NICAM

1 simulation to prepare realistic atmospheric fields in the mesosphere for 0000 UTC on March

2 17, 2015. The latter 3-D analyzed fields were only used at above 0.1 hPa, as variables of vertical

3 pressure velocity, cloud liquid water and ice mixing ratios are not included. Vertical pressure

4 velocities, cloud liquid water and ice mixing ratios above 0.1 hPa are set to zero. A time

5 integration was performed until 0000 UTC on March 24. The time step was 15 seconds. As

6 part of the boundary layer scheme, MYNN level 2 (Nakanishi and Niino, 2004) was used. No

7 cumulous or gravity wave parameterization was employed. The model output was recorded

8 every 1 hour. It should be noted that this model does not use the nudging method as an external

9 forcing for the atmospheric component.

11 **3. Observational results**

12   Figure 2a shows the time-height section of the line-of-sight wind velocity observed by the

13 east beam of the PANSY radar system. In the lower stratosphere, wavy structures with short

14 vertical wavelengths are shown. Shibuya et al. (2015) showed that such a structure observed in

15 May of 2013 at Syowa Station was due to inertia-gravity waves with a vertical wavelength of

16 about 2 km. In the mesosphere, strong echoes were detected at heights of 60 km to 80 km over

17 this time period. These polar mesosphere winter echoes (PMWEs) are likely intiated by

18 increased ionization during the solar flare event occurring on March 17-18, 2015 (Kataoka et

19 al. 2015; Jacobsen and Andalsvik 2016; Cherniak and Zakharenkova 2016). In this period, the

20 polar night jet was in the phase of formation around Syowa Station at the stratopause (at the

21 height of about 55 km, not shown). As is shown in Figure 2a, strong wave-like disturbances

22 were observed in the mesosphere. Figures 2b and 2c, respectively show line-of-sight wind

23 velocities of the east and west beams at heights of 65 - 80 km for 00 UTC on March 21 to 00

24 UTC on March 24. In Figures 2b and 2c, it is clear that phases of dominant disturbances

25 propagate downward; a vertical phase velocity (broken line) and an observed period (a green

26 arrow) are about $-0.3$ m s$^{-1}$ and 12.3 h, respectively. This indicates that the vertical wavelength

1 is about 13.8 km.

2     As the zenith angle of tilted beams of the PANSY radar system is $\theta = 10°$, locations of

3 the observation points by opposite beams in the mesosphere are separated by approximately 25

4 km at a height of 70 km. Figures 3a and 3b show time-height sections of estimated zonal and

5 meridional wind components.

6     Based on the working hypothesis that wind disturbances in the mesosphere are due to

7 inertia-gravity waves, wave parameters are estimated using a hodograph analysis. A hodograph

8 analysis (e.g., Hirota and Niki 1986; Sato 1994) is applied to wind fluctuations at heights of

9 73.2 km, 73.8 km and 74.4 km for March 22 and at the heights of 70.8 km, 71.4 km and 72.0

10 km for March 23. In this analysis, hodographs are made in the time direction.

11     First, wave zonal ($u'$) and meridional ($v'$) wind fluctuations were fitted to sinusoidal

12 functions as follows:

$$u' = \hat{u}\sin(\omega t + \theta_u) + u_{\text{o}}$$
$$v' = \hat{v}\sin(\omega t + \theta_v) + v_{\text{o}},$$

(1)

13 where $\hat{u}$ and $\hat{v}$ are the amplitudes of $u'$ and $v'$, respectively, $\omega$ is the observed wave

14 frequency, $t$ is time, $\theta_u$ and $\theta_v$ are phases of zonal and meridional wind fluctuations, and $u_{\text{o}}$

15 and $v_{\text{o}}$ are offsets of zonal and meridional wind fluctuations, respectively. Parameters ($\hat{u}$, $\hat{v}$,

16 $\omega$, $\theta_u$, $\theta_v$, $u_{\text{o}}$ and $v_{\text{o}}$) are determined using a nonlinear least square method so that the

17 residual $\sqrt{(u'_{\text{obs}} - u')^2 + (v'_{\text{obs}} - u')^2}$ is smallest. Figure 4 shows a time series of observed

18 horizontal wind fluctuations and results of the fitting at 70.8 km and 72.0 km for March 23. It

19 is clear that the observed wind fluctuations seem to have a sinusoidal form with a period of

20 about 12 h, and the fitting is successful. Moreover, phases of zonal and meridional wind

21 fluctuations at 72.0 km seem to be advanced compared to those at 70.8 km. Using these phase

22 differences in zonal and meridional wind fluctuations, vertical wavenumbers for zonal and

23 meridional fluctuations are estimated, respectively. Table 1a summarizes parameters such as

1    wave frequencies, vertical wavenumbers and vertical phase velocities estimated from $u'$ and

2    $v'$. The estimated period ranges from 11.0 h to 13.8 h, which is quasi 12 h. The estimated

3    vertical wavelengths are 12.0 km and 8.5 km for $u'$ and $v'$ for March 22 and are 15.4 km and

4    12.3 km for $u'$ and $v'$ for March 23, respectively. Thus, the vertical phase velocities are

5    −0.26 m s$^{-1}$ and −0.19 m s$^{-1}$ for $u'$ and $v'$ for March 22 and −0.35 m s$^{-1}$ and −0.28 m s$^{-1}$ for

6    $u'$ and $v'$ for March 23, respectively. Although the estimation based on $v'$ for March 22

7    shows slightly different values, the vertical phase velocities and observed periods agree well

8    with the rough estimation denoted by broken lines and the green arrow in Figs. 2b and 2c,

9    respectively (approximately −0.3 m s$^{-1}$ and 12.3 h).

10    The linear theory of inertia-gravity waves indicates that a hodograph is ellipse-shaped

11    (e.g., Shibuya et al., 2015). The lengths of major and minor axes of the hodograph ellipse

12    correspond to the amplitudes of horizontal wind components, which are parallel ($u_\parallel$) and

13    orthogonal ($u_\perp$) to the horizontal wavenumber vector ($\overrightarrow{k_h}$), respectively. The components of

14    $u_\parallel$ and $u_\perp$ are written using the zonal ($u'$) and meridional ($v'$) wind fluctuations:

$$u_\parallel = u' \cos \alpha + v' \sin \alpha$$
$$u_\perp = -u' \sin \alpha + v' \cos \alpha, \tag{2}$$

15    where $\alpha$ is the angle of $u_\parallel$ measured clockwise from the east. Based on the polarization

16    relation, the intrinsic frequency $\widehat{\omega}$ can be determined from the ratio of the lengths of the major

17    to minor axes:

$$\widehat{\omega} = \left| \frac{u_\parallel}{u_\perp} f \right|, \tag{3}$$

18    where $f$ denotes the inertial frequency. The intrinsic frequency is taken to be positive without

19    losing generality (e.g., Sato et al., 1997).

20    The direction of the vertical energy propagation can be estimated from the rotation of the

21    hodograph in the vertical direction as follows: in the Southern Hemisphere, a counterclockwise

22    (clockwise) rotation with increasing height denotes upward (downward) energy propagation.

1    Hodographs in the vertical direction for 1200 UTC on March 22 and for 1200 UTC on March

2    23 show counterclockwise rotation (not shown), indicating upward energy propagation as also

3    shown in Fig. 4. This also means that the vertical wavenumber $m$ is negative.

4         The horizontal wavenumber $\left|\overrightarrow{k_h}\right|$ can be indirectly estimated using the dispersion

5    relation of inertia-gravity waves, though an ambiguity for $180°$ remains in the direction of the

6    horizontal wavenumber vector. For hydrostatic inertia-gravity waves, the dispersion relation in

7    a uniform background is written as follows:

$$\left|\overrightarrow{k_h}\right| = \sqrt{\frac{(\hat{\omega}^2 - f^2)m^2}{N^2}}, \qquad (4)$$

8    where $N$ is the Brunt-Väisälä frequency. Here, as a typical value, $N^2 = 3.0\times10^{-4}$ s$^{-2}$ for the

9    mesosphere was used. The zonal and meridional wavenumbers $(k, l)$ are determined as $k =$

10   $\pm\left|\overrightarrow{k_h}\right| \cos \alpha$, and $l = \pm\left|\overrightarrow{k_h}\right| \sin \alpha$, respectively. The plus-minus sign here denotes the

11   ambiguity of the wavenumber vector.

12        Figure 5 shows hodographs of the fitted sinusoidal fluctuations at heights of 70.8 km and

13   72.0 km for March 23. The intrinsic frequency and zonal and meridional wavenumbers are

14   estimated from Eqs. (3) and (4), respectively. Table 1b presents the fitted amplitude of zonal

15   and meridional wind fluctuation and estimated wave parameters resulting from the hodograph

16   analysis.Wavenumbers are directed eastward (or westward) or northeastward (or

17   southwestward). Parameter $f/\hat{\omega}$ ranges from 0.6 to 0.85. Horizontal wavelengths of the best

18   fitted parameters are longer than 1100 km, indicating that these fluctuations are due to relatively

19   large-scale inertia-gravity waves. Thus, the applied assumption on the homogeneity of

20   observed winds by dual beams (Section 2.1) is justified. Uncertainties of estimated wind

21   amplitude and other related wave parameters are also estimated using residuals of the nonlinear

22   least squares fitting and assuming on the assumption that the uncertainties in the estimates of

23   the zonal and meridional wind amplitude are the same. It seems that the estimated horizontal

1 wavelength at a height of 70.8 km for March 23 has a relatively large uncertainty ($|2\pi/\overrightarrow{k_h}| =$

2 $990 \sim 7778$). However, it should be noted that the case for the largest horizontal wavelength

3 corresponds to a case with $\hat{\omega} \sim f$ (i.e. close to the inertial oscillation) and hence its ambiguity

4 is large for the wavelength ($|\overrightarrow{k_h}| \sim 0$).

6 ## 4. Numerical experiment results

7 ### 4.1. Simulated wave structures

8     To examine spatial structures and generation mechanisms of the inertia-gravity waves, a

9 model simulation based on the NICAM was performed. Figure 6a shows the time-height

10 section of the simulated winds ($u \sin\theta + w \cos\theta$ (where $\theta = 10°$)) for Syowa Station from

11 00 UTC on March 17 to 00 UTC on March 24, 2015, reflecting the line-of-sight velocity of the

12 east beam of the PANSY radar system. A comparison with the observations (Fig. 2) shows that

13 the model successfully simulated synoptic-scale disturbances in the troposphere, although

14 phases of these disturbances vary slightly from observations near the end of the simulation. In

15 the lower stratosphere, a wavy structure with a small vertical wavelength of less than about 2

16 km, which was observed by the radar system from 00 UTC on March 17 to 00 UTC on March

17 20, is hardly shown in Fig. 6a. This may be attributable to the large vertical spacing ($\Delta z = 400$

18 m) of the model compared to such a short vertical wavelength. From the middle stratosphere

19 to the mesosphere, downward-propagating large-amplitude disturbances are dominant, which

20 is consistent with the observations. Figures 6b and 6c show the line-of-sight velocity of the east

21 beam and the zonal wind component for the same time and height sections as those reflected

22 in Figs. 2b and 2c, respectively. The amplitude of these disturbances is also comparable to that

23 of the observations; for example, the amplitude of the zonal wind component at a height of

24 about 70 km for 12 UTC on March 23 is approximately 30 m s$^{-1}$, which agrees with the

25 observations (see Figs. 4a and 4c).

26     Figure 7a shows the time-height section of anomalies of zonal wind components from the

1  time average at each height. As is shown in Fig. 6b, wave-like structures for the observation

2  period of about 12 h seem dominant in the mesosphere which is consistent with the radar

3  observation (Fig. 2b). Thus, we first examined diurnal and semi-diurnal migrating tidal

4  components, which are defined as components for wave period $\tau = 24$ h and zonal

5  wavenumber $s = 1$ and for $\tau = 12$ h and $s = 2$, respectively. Figure 7b shows the time-

6  height section of diurnal and semi-diurnal migrating components of zonal winds. Surprisingly,

7  these components are not dominant even in the mesosphere. Figure 7c shows the time-height

8  section of zonal wind components of planetary wave components, which are defined as

9  components with $\tau \geq 42$ h. This component does not seem to be dominant in the mesosphere.

10 Moreover, we examined the amplitude of small-scale gravity waves, which are defined as

11 components with horizontal wavelengths of less than 1000 km, as occasionally shown by

12 previous studies (e.g., Geller et al., 2013). In this study, a spatial filter is applied to the x-y

13 coordinate centered at the South Pole as projected by the Lambert azimuthal equal-area

14 projection. Figure 7d shows the time-height section of zonal wind components of the small-

15 scale gravity waves. Although these small-scale gravity waves sometimes have amplitudes that

16 exceed 20 m s$^{-1}$ in the mesosphere, the wave structures shown in Fig. 7a are not fully explained.

17     The remaining component is shown in Fig. 7e. This component has a quite similar

18 structure and amplitude to the unfiltered anomalies shown in Fig. 7a. These results suggest that

19 dominant wave structures in the mesosphere did not form due to migrating tides, planetary

20 waves or small-scale gravity waves, but due to the remaining component. The remaining

21 component has a horizontal wavelength of greater than 1000 km and wave periods of less than

22 42 h. We further examined characteristics of the remaining component such as horizontal and

23 vertical wavenumbers and intrinsic and observed wave frequencies.

24     Figure 7e shows several large-amplitude wave packets over Syowa Station. The envelope

25 function of the wave packets is examined using an extended Hilbert transform method proposed

by Sato et al. (2013). An extended Hilbert transform $H[a(x,t)]$ is a fluctuation field composed of a Fourier component of a particular fluctuation field $a(x,t)$ whose phase is shifted by $-\pi/2$ radians. An envelope function $A_{\text{env}}(x,t)$ of $a(x,t)$ is obtained using $a(x,t)$ as follows:

$$A_{\text{env}}(x,t) = \sqrt{a(x,t)^2 + H[a(x,t)]^2}. \qquad (5)$$

The extended Hilbert transform must be applied in one direction in time or space where waves are fluctuating (including at least more than two wave crests). In this study, envelope functions are estimated using the extended Hilbert transform of the time direction.

Figure 8 shows the envelope functions calculated using the extended Hilbert transform applied to remaining components shown in Fig. 7e. Several large-amplitude wave packets are identified and labeled as (i) to (v) for further wave parameter estimation. The observed wave period and the vertical wavelength of each packet are estimated directly in Fig. 7e. The zonal wavelengths and phase velocities are directly estimated using Hovmöller diagrams. Figure 9 shows the Hovmöller diagram at a height of 70 km at 69°S. A lot of wave packets appear not only over Syowa Station throughout the simulation period, except for the initial day of the time integration. It is clear that most waves propagate westward. At a longitude of roughly 40°E (green dashed line) where Syowa Station is located, some dominant wave packets are found as is shown in Fig. 8, corresponding to packets (i) for March 19, (ii) March 20 and (v) March 22, respectively.

In addition, to examine horizontal structures of the wave packets, we created composite maps of zonal wind components. The composite is calculated for the time period denoted by green rectangles in Fig. 8. For each wave packet, the locations with the local maxima of the zonal wind components near Syowa Station along a latitude of 69°S are chosen as reference points for the composite. In other words, horizontal maps of zonal wind wave components are moved in the zonal direction and are then averaged. Thus, this composite shows an averaged

1  phase structure of zonal wind wave components near Syowa Station. The results are shown in

2  Figs. 10a to 10e for packets (i) to (v), respectively. It seems that wave structures are evident for

3  all packets near Syowa Station. From features observed in the time-height section, the

4  Hovmöller diagram and the composite maps of zonal wind components, we directly estimated

5  wave parameters of horizontal wavelengths, vertical wavelengths, observed frequencies, zonal

6  phase speeds, vertical phase speeds and intrinsic frequencies, which are summarized in Table

7  2.

8      The vertical phase speeds, observed wave periods and vertical wavelengths obtained from

9  the model simulation data agree quite well with those obtained from the PANSY radar

10  observations. Moreover, directly estimated zonal and meridional wavenumbers from the

11  simulation (Table 2) also agree quite well with those indirectly estimated from PANSY radar

12  observations using polarization and dispersion relations of inertia-gravity waves (Tables 1a and

13  1b). In addition, it is important to note that wave parameters ($\omega$, $\vec{k}$ and $m$) of packets (i) to

14  (v) are consistent with the dispersion relation of the hydrostatic inertia-gravity waves:

$$\hat{\omega}^2 = (\omega - \vec{U} \cdot \vec{k})^2 = f^2 + \frac{N^2 |\vec{k}|^2}{m^2}, \qquad (6)$$

15  where $\omega$ is the ground-based frequency, $\vec{k} = (k, l)$ and $m$ are horizontal and vertical

16  components for the wavenumber vector, respectively, and $\vec{U}$ is the background horizontal

17  wind vector. Intrinsic frequencies $\hat{\omega}$ obtained from the model simulation using Eq. (6) also

18  agree with those obtained from the PANSY radar observation. From these results, we conclude

19  that dominant half-day wave period fluctuations observed in the mesosphere are likely

20  attributable to large-scale inertia-gravity waves. Hereafter, we refer to the remaining

21  component as "large-scale inertia-gravity waves."

23  **4.2. Wave propagation and generation mechanism**

24      In this section, we examine the origins of the large-scale inertia-gravity waves simulated

25  near Syowa Station. In particular, we examine disturbances occurring over wave periods of

close to 12 h, which were extracted by applying a bandpass filter with cutoff wave periods of 6 h and 24 h to large-scale inertia-gravity waves. It is confirmed that this spectral range of the bandpass filter is narrow enough to extract the large-scale inertia-gravity waves clearly.

Case studies are conducted for wave packets (i) and (v), as they show clear wave structures at the height of 70 km, where the PANSY radar system observed inertia-gravity waves. The propagation of wave packets identified using the extended Hilbert transform method is manually traced. Three dimensional locations of the wave packets are determined by the maxima of the envelope function for each time. Hereafter, we refer to this method as "manual wave packet tracing". The advantage of this method is that a specific location of a possible wave source can be directly examined.

The approach of the manual wave packet tracing for packet (v) is illustrated in Figs. 11a and 11b, which show horizontal maps of zonal wind components of the large-scale inertia-gravity waves and their envelope functions for 03 UTC on March 23 and a Hovmöller diagram at 69°S. Significant wave disturbances with large amplitudes are observed near Syowa Station corresponding to packet (v). The location of packet (v) (green circles in Figs. 11a and 11b) is estimated in the following: First, the time when the envelope function of packet (v) takes its local maximum in the Hovmöller diagram (Fig. 11b) is determined. Second, the location of packet (v) at that time is determined to where the envelope function has its local maximum in the horizontal map (Fig. 11a). Figures 11c and 11d show the results for packet (i). By repeating this procedure at an interval of about 1 km in the vertical direction, temporal and spatial locations for a particular packet are manually estimated. For this tracing, the Hovmöller diagram is examined at the latitude of the wave packet location in the former procedure.

Figures 12a-d show the time and the spatial locations of packet (v) at heights of 60 km, 40 km, 25 km and 23 km, respectively. It appears that the location of packet (v) is successfully traced backward from a height of 70 km to 23 km, suggesting that packet (v) observed over

1   Syowa Station in the mesosphere propagated from the lower stratosphere at roughly (100°E,

2   40°S). At heights of 25 km to 23 km, the vertical propagation of packet (v) is quite slow

3   compared to that in the upper stratosphere and mesosphere.

4       Figures 12e to 12 g show the times and spatial locations of packet (i) at heights of 63 km,

5   58 km, 53 km and 48 km, respectively. At heights of 70 km, 63 km and 58 km, the green circles

6   seem to trace the same wave structures. However, as we cannot trace packet (i) below a height

7   of 53 km, the wave structure becomes obscured at heights of 53 km and 48 km.

8       To confirm the validity of the manual wave packet tracing results, we conducted a

9   backward ray tracing analysis of the large-scale inertia-gravity wave (e.g., Marks and

10  Eckermann 1995). We used the wave parameters of packets (i) and (v) shown in Table 2 as

11  initial parameters for the ray tracing analysis. The average of the model output for March 17 to

12  March 23 is used as the background wind for the ray tracing analysis. Figure 13 and Table 3

13  summarize the manual packet and ray tracing results. The times and spatial locations of packet

14  (v) detected by the manual packet tracing agree with those obtained by idealized ray tracing,

15  although not for the lower stratosphere. However, the tracing of packet (i) agrees with those by

16  idealized ray tracing results at above 58 km where clear wave structures are shown in the

17  horizontal map, although the idealized ray slowly travels at right angles to the manual ray.

18  These findings support the validity of manual wave packet tracing based on the extended

19  Hilbert transform and ray tracing based on inertia-gravity wave theory.

20      The source of the inertia-gravity waves can be located at any altitude along the ray above

21  the lowest traceable altitude. Thus, we further examine possible sources of packets (i) and (v)

22  along the ray shown in Fig. 13. First, we focus on the ray of packet (v) in the lower stratosphere.

23  Figure 14 shows the longitude-height section of background winds below $z = 18$ km and of

24  disturbances above $z = 19$ km at 40°S for 03 UTC on March 21. At roughly 100°E longitude,

25  wave disturbances appear to be captured over the core of the tropospheric jet stream. This

1  feature is quite similar to the gravity waves generated by the spontaneous radiation from the

2  large-scale jet in the tropopause (e.g., O'Sullivan and Dunkerton, 1995; Plougonven and

3  Synder 2007; Yasuda et al., 2015a, b). The long propagation time in the lower stratosphere may

4  be related to the wave capture mechanism (Bühler and McIntyre, 2005; Shibuya et al., 2015).

5      To explore such a possibility, a horizontal map of the residual of the nonlinear balance

6  equation ($\Delta NBE$; Zhang et al., 2001), which is an index showing the degree of flow imbalance,

7  is examined. Here, $\Delta NBE$ is defined as follows:

$$\Delta NBE = 2J(u,v) + f\varsigma - \alpha\nabla^2 P \qquad (7)$$

8  where $\varsigma$, $\alpha$, and $P$ denote the relative vorticity, specific volume and pressure level,

9  respectively. The Jacobian term is $J(u,v) = \partial u/\partial x \times \partial v/\partial y - \partial v/\partial x \times \partial u/\partial y$. To exclude

10  possible contaminations of $\Delta NBE$ by small-scale gravity waves, we apply a low-pass filter in

11  the zonal and meridional directions with a cutoff length of 1000 km in advance. Figure 15

12  shows horizontal maps of the absolute value of the horizontal wind and $\Delta NBE$ at a height of

13  10 km for 03 UTC on March 21. The absolute value of the horizontal wind is also denoted by

14  thick contours. It is clear that large values are observed in $\Delta NBE$ around the tropospheric jet

15  meandering around (110°E, 40°S), where packet (v) was located. This feature not only suggests

16  that the imbalance in the tropospheric jet was significant but also that packet (v) may have been

17  generated by the spontaneous radiation mechanism.

18      Next, we examined a possible generation mechanism for packet (i). The disappearance of

19  the clear wave structure at a height of 53 km (Figs. 12f and 12g) may indicate that the source

20  of packet (i) is found at this height. A plausible generation mechanism of inertia-gravity waves

21  in the upper stratosphere is spontaneous radiation from the polar night jet (e.g., Sato and

22  Yoshiki, 2008). It is also worth noting that observational studies show high percentages of

23  downward gravity wave propagation in the polar stratosphere compared to those found at low

24  and middle latitudes (e.g., Yoshiki and Sato, 2000; Guest et al., 2000; Moffat-Griffin et al.,

1   2013; Murphy et al., 2014; Mihalikova et al., 2016). To confirm this possibility, we examined

2   fluctuation characteristics and background zonal winds of the upper stratosphere. Figure 16

3   shows a longitude-height cross-section of fluctuation components ($\sqrt{\rho_0}u'$) and the background

4   zonal wind at 15 UTC on March 18 at 65°S. The background zonal wind is obtained using a

5   low-pass filter with a cutoff zonal wavelength of approximately 5,000 km.

6       Interestingly, it seems that fluctuations show symmetric features above and below the core

7   of the polar night jet at a height of 50 km. The height at which packet (i) becomes obscured

8   roughly corresponds to the core of the polar night jet (Figs. 12f and 12g). These results imply

9   that fluctuations are generated at a height close to the core of the polar night jet. To confirm

10   this, we examined the vertical profile of the energy flux $\overline{p'w'}$ (Fig. 16b). The average was

11   calculated for the longitudinal region spanning from -90°E to 60°E. The energy flux is upward

12   above and downward below the core of the polar night jet. This result supports the hypothesis

13   that packet (i) was generated at a height close to the core of the polar night jet.

14       This symmetric phase structure observed in Fig. 16a is similar to the structures from the

15   theoretical studies of spontaneous radiation of inertia-gravity waves from a balanced flow (e.g.,

16   Yasuda et al., 2015b: their Figure 6). Yasuda et al. (2015a, b) proposed that the quasi-resonance

17   of gravity waves and a secondary circulation slaved to a balanced jet flow serves as the

18   spontaneous radiation mechanism. The study showed that the quasi-resonance occurs when

19   ground-based wave periods of radiated gravity waves are comparable to the time-scale of the

20   slaved motion due to a significant Doppler shift by the strong and balanced flow. Moreover, a

21   time-scale in which a fluid particle travels over a descent-ascent couplet structure (i.e., half of

22   an intrinsic period of a radiated gravity wave; $\hat{\tau}$) needs to be shorter than half of the inertial

23   period. This corresponds to the condition that the Lagrangian Rossby number ($R_{\mathrm{Lagr}}$) is greater

24   than unity, which was discussed in McIntyre (2008). Spontaneously radiating inertia-gravity

25   waves have a shorter wavelength leeward of the jet streak through the wave capture mechanism

1    (Bühler and McIntyre, 2005). Yasuda et al. (2015a, b) also showed that the source term formula

2    of radiated gravity waves by the quasi-resonance is equal to $\Delta NBE$. However, a large $\Delta NBE$

3    was not observed in the upper stratosphere and mesosphere for the case examined in the present

4    study. The polar night jet around an approximate height of 55 km did not have the strength

5    and/or did not meander enough to cause a large $\Delta NBE$ (not shown). Thus, a different

6    mechanism needs to be considered to explain the spontaneous radiation of gravity waves in the

7    upper stratosphere and mesosphere.

8         Taking into account the fact that the time-variation of the westerly jet around 55 km is

9    mainly caused by migrating tides, we propose a new mechanism for the spontaneous radiation

10   in the upper stratosphere and mesosphere. Figure 17 shows the schematic illustration. Figure

11   17a shows anomalies of $\theta$ from the zonal mean and vertical wind couplets associated with a

12   semi-diurnal migrating tide at the height of the core of the polar night jet in the longitudinal

13   direction. As vertical winds are adiabatically present along the modulated $\theta$ surface, a

14   mountain-wave-like generation that was discussed in the previous studies may occur. In this

15   case, the vertical winds oscillate with a period of 12 h due to the time variation of the $\theta$ surface

16   associated with the semi-diurnal migrating tide. The deformation of the $\theta$ surface is not

17   caused by the slaved components of the large-scale balanced flow, and hence $\Delta NBE$ is not

18   necessarily large. An intrinsic period $\hat{\tau}$ for this case is calculated as $\hat{\tau} = {L}/{(U + U_{\text{tide}})}$,

19   where $L$ is a half-length of the latitude circle, $U$ is a speed of the zonal wind and $U_{\text{tide}}$ is a

20   ground-based phase speed of the semi-diurnal tide. Since ${L}/{U_{\text{tide}}}$ is 12 h, $\hat{\tau}$ is less than a half

21   of the inertial period in the westerly background wind ($U > 0$). Therefore, gravity waves with

22   a period of 12 h are likely radiated around the jet core. In addition, because of the horizontal

23   shear of the background wind including the migrating tides, the wave-capture can occur to

24   cause the horizontal wavelength of the radiated gravity waves to be less than that of the semi-

25   diurnal migrating tide, which was observed.

Next, we confirm if the patterns of $\theta$ anomalies and vertical velocities associated with the migrating tides are seen in the simulation data. Figure 18a shows the Hovmöller diagram of $\theta$ anomalies and vertical velocities associated with the diurnal and semi-diurnal migrating tides at a height of 55 km at 65°S. The phase relation of $\theta$ and vertical velocities are adiabatic, which is consistent with the scenario shown in Fig. 17a. The $\theta$ anomalies associated with the semi-diurnal tide seem modulated and partly amplified by the presence of the diurnal migrating tide. Figure 18b shows the Hovmöller diagram of $\theta$ and vertical winds of the large-scale gravity wave components, overlaid by the background zonal wind. Note that the background zonal wind is largely modulated by the migrating tides. It is interesting that packet (i) seems to be generated near 30°E at about 12 UTC when the packet is located downstream of the zonal wind maxima, which is consistent with the source location and generation timing estimated by the manual packet tracing method. This fact suggests that the wave capture mechanism is acting in association with the migrating tides. This is the most likely mechanism of packet (i) generation.

We also examined sources of other wave packets (ii), (iii) and (iv) and of other wave packets that are dominant at different longitudes (Fig. 9). The results suggest that these wave packets were also generated by spontaneous radiation from the upper tropospheric jet stream or from the polar night jet stream (not shown in detail).

## 5. Discussion

As is shown in Section 4, wave structures with large amplitudes in the lower mesosphere (below 80 km) with the ground-based period of quasi 12 h are likely attributable to large-scale inertia-gravity waves. The horizontal wavelengths of quasi 12 h inertia-gravity waves range from 1500 km to 2500 km as shown in Table 2. This conclusion diverges from suggestions made in previous studies, which posit that 12 h disturbances can be either migrating semi-diurnal tides of zonal wavenumber two or non-migrating semi-diurnal tides of zonal

wavenumber one. This difference can be attributed to the difference in observed height regions as follows: height regions examined in this study include the upper stratosphere and lower mesosphere below 80 km while those examined in previous studies include the mesosphere located above 85 km.

Large-scale inertia-gravity waves with horizontal wavelengths of longer than 1000 km in the mesosphere have already been reported in several studies (Li et al., 2007; Lu et al., 2009, Nicolls et al., 2010; Chen et al., 2013). For example, Nicolls et al. (2010), using the Poker Flat Incoherent Scatter Radar system, found large-amplitude coherent wave packets with wave periods of roughly 10.5 h and horizontal wavelengths of 700 km to 1600 km in the mesosphere. Nicolls et al. (2010) cited jet stream adjustment in the tropopause as a potential source. Chen et al. (2013) also estimated a source for one inertia-gravity wave with a horizontal wavelength of 2200 km, a period of 7.7 hour and a vertical wavelength of 22 km, which was observed in the Antarctic mesopause region by combined Fe lidar/MF radar measurements. They heuristically traced the inertia-gravity wave back to a region of unbalanced flow in the stratosphere (z ~ 43 - 46 km). However, no previous studies have directly examined sources of these large-scale inertia-gravity waves in the mesosphere using a numerical model. This study examines the propagation of such large-scale inertia-gravity waves and generation by spontaneous radiation from the polar night jet and tropospheric jet, combining the observational data and numerical simulation outputs.

Recently, Sato et al. (2017) showed that zonal (meridional) momentum flux spectra at the summer mesosphere over Syowa Station are mainly positive (negative), and an isolated peak of the momentum fluxes is observed near a frequency of 12 hour, using continuous observations of polar mesosphere summer echoes at heights from 81–93 km by the PANSY radar. The signs of momentum flux suggests that gravity waves propagate from low latitude regions on the assumption of upward propagation. Yasui et al. (2016) also suggested that gravity waves in the

1     summer mesosphere may originate from the tropical convections using the MF radar

2     observation at Syowa Station. Sato et al. (1999) indicated that such meridional propagation of

3     the inertia-gravity waves from the low latitude region and the critical-level filtering mechanism

4     can explain the isolated energy peak near the inertia-frequency (near a frequency of 12 hour at

5     Syowa Station). Moreover, the tide-induced spontaneous radiation mechanism proposed in this

6     study implies frequent generations of quasi 12 h inertia-gravity waves at the polar vortex.

7     Further studies are needed to clarify physical mechanisms for the existence of the isolated

8     energy peak near 12 hour in the mesosphere at Syowa Station.

9        We have further examined vertical fluxes of zonal and meridional momentum associated

10    with large-scale inertia-gravity waves $\rho_0 \overline{u'w'}$ and $\rho_0 \overline{v'w'}$. The overbar denotes a zonal

11    averaging operation. Figures 19a and 19b show latitude-height sections of $\rho_0 \overline{u'w'}$ and $\rho_0 \overline{v'w'}$,

12    respectively, which are averaged for March 19 to March 23 2015. Large negative $\rho_0 \overline{u'w'}$ and

13    $\rho_0 \overline{v'w'}$ values are distributed approximately 40°S in the lower stratosphere and approximately

14    75°S in the mesosphere. The signs of $\rho_0 \overline{u'w'}$ and $\rho_0 \overline{v'w'}$ are consistent with parameter

15    estimations from PANSY radar observations and from the numerical simulation. The slanted

16    structures seem quite similar to the propagation path of packet (v) discussed in Section 4.2.

17    Such a slanted structure is likely formed from the meridional propagation of inertia-gravity

18    waves, which is numerically shown and theoretically discussed by Sato et al. (2009) and Sato

19    et al. (2012) in terms of refraction and advection by background wind.

20        Interestingly, Fig. 19a shows that the value of $\rho_0 \overline{u'w'}$ is lower in the middle stratosphere,

21    thus showing a peak of negative $\rho_0 \overline{u'w'}$ in the mesosphere. Small-scale gravity waves do not

22    follow such a pattern (not shown). This result suggests that parts of large-scale inertia-gravity

23    waves are generated in the upper stratosphere as discussed in Section 4.2. In contrast, such a

24    feature is not observed in $\rho_0 \overline{v'w'}$, although a small negative local maximum is present at

25    heights of 50 km to 55 km at approximately 60°S. This result implies that wavenumber vectors

1    of inertia-gravity waves in the mesosphere tend to move eastward, consistent with the

2    parameter estimation shown in Section 4.1.

3        Next, we examined the energy density of the large-scale inertia-gravity waves by dividing

4    the total energy density into the following three components: horizontal wind kinetic energy

5    ($\overline{KE}$), vertical wind kinetic energy ($\overline{VE}$) and potential energy ($\overline{PE}$):

$$\overline{KE} = \frac{1}{2}\rho_0\left(\overline{u'^2} + \overline{v'^2}\right), \tag{8}$$

$$\overline{VE} = \frac{1}{2}\rho_0\overline{w'^2}, \tag{9}$$

and
$$\overline{PE} = \frac{1}{2}\rho_0\frac{g^2}{N^2}\overline{\left(\frac{T'}{T}\right)^2}. \tag{10}$$

6    According to the linear theory of hydrostatic inertia-gravity waves, the ratio of $\overline{VE}$ to $\overline{PE}$ has

7    the following relation (from the thermodynamic equation) (e.g., Wang et al., 2005; Geller and

8    Gong 2010, Geller et al., 2013);

$$\frac{\overline{VE}}{\overline{PE}} = \frac{\widehat{\omega}^2}{N^2}. \tag{11}$$

9    Thus, $|f/\widehat{\omega}|$ can be derived as follows:

$$\left|\frac{f}{\widehat{\omega}}\right| = \left|\frac{f}{N}\right|\sqrt{\frac{\overline{PE}}{\overline{VE}}}. \tag{12}$$

10       Figure 19c shows the latitude-height section of $|f/\widehat{\omega}|$. In the mesosphere, $|f/\widehat{\omega}|$ ranges

11   from 0.6 to 0.8 at approximately 70°S, which agrees quite well with estimates from the

12   hodograph analysis (Tables 1 and 2). The fact that $|f/\widehat{\omega}|$ has higher values than 0.6 indicates

13   that the large-scale inertia-gravity waves are almost hydrostatic. Note that the value of $|f/\widehat{\omega}|$

14   is larger than 1.0 in the lower stratosphere, which is inconsistent with the linear theory of

15   inertia-gravity waves. This implies that the large-scale inertia-gravity waves defined in Section

16   4.1 include balanced components in the lower stratosphere (e.g., baroclinic wave components)

17   as well as large-scale inertia-gravity waves.

18       Figures 19d and 19e show latitude-height sections of $\overline{KE}$ and $\overline{PE}$ for the large-scale

1    inertia-gravity waves. The slanted structures in Figs. 19a and 19b are also shown in Figs. 19d

2    and 19e. It should be noted that the ratio of the Coriolis parameter to the intrinsic frequency

3    $(f/\hat{\omega})$ can also be obtained from $\overline{KE}$ and $\overline{PE}$ as follows:

$$\left|\frac{f}{\hat{\omega}}\right| = \sqrt{\frac{\frac{\overline{KE}}{\overline{PE}} - 1.}{\frac{\overline{KE}}{\overline{PE}} + 1}}. \tag{13}$$

4    We confirmed that $(f/\hat{\omega})$ values obtained by Eq. (13) are consistent with the result obtained

5    from Eq. (12) (not shown).

7    **6.  Summary**

8        The first observation with a complete system of the PANSY radar were successfully

9    performed for March 16 – 24, 2015. During this period, quasi 12 h disturbances in the

10   mesosphere at heights of 70 km to 80 km were detected by the PANSY radar system. Our main

11   results are summarized as follows:

12       1)       The observed wave period and vertical wavelength are about 12.3 h and 13.8

13           km, respectively. The estimated horizontal wavelength is longer than 1100 km. The

14           wavenumber vectors tend to be directed northeastward or southwestward. Ratios of the

15           Coriolis parameter to the intrinsic frequency range from 0.6 to 0.85.

16       2)       Moreover, using the non-hydrostatic numerical model with a model top of 87

17           km, we succeeded in simulating quasi 12 h disturbances in the mesosphere. Using time

18           and spatial filters, we found that quasi 12 h disturbances are not attributable to semi-

19           diurnal migrating tides, but to large-scale inertia-gravity waves with horizontal

20           wavelengths of longer than 1400 km. Wavenumber vectors simulated in the NICAM are

21           directed northeastward. Wave parameters directly estimated using the NICAM agree

22           quite well with those estimated by the PANSY radar observation system.

23       3)       The detected inertia-gravity waves were likely generated by the spontaneous

radiation mechanism of the mid-latitude upper tropospheric jet at the tropopause or the polar night jet. Inertia-gravity waves generated near the mid-latitude tropopause propagate laterally and vertically to the polar mesosphere.

4)    A new spontaneous radiation mechanism associated with the semi-diurnal migrating tides is proposed. This mechanism explains a radiation of inertia-gravity wave with a period of 12 h in the upper stratosphere and mesosphere. The wave-capture mechanism is important downstream of a zonal wind maxima caused by the migrating tides.

5)    Vertical fluxes of the zonal and meridional momentum of large-scale inertia-gravity waves show a slanted structure from the mid-latitude lower stratosphere to the polar mesosphere. Moreover, the vertical flux of the zonal momentum shows a strong negative peak in the mesosphere, suggesting the generation of large-scale inertia-gravity waves in the upper stratosphere.

The present study offers a quantitative discussion based on high-resolution observations and numerical models. Statistical analyses of large-scale inertia-gravity waves in the real atmosphere will be of interest as future studies using observations and numerical simulations in the different seasons.

## 7.  Data availability

The PANSY radar observation data is available at the project website, http://pansy.eps.s.u-tokyo.ac.jp. Model outputs are available on request from the corresponding author.

## 8.  Competing interest

The authors declare that they have no conflict of interest.

## Acknowledgements

The PANSY multi-institutional project operated by the University of Tokyo and the National Institute of Polar Research (NIPR), and the PANSY radar system was operated by the Japanese Antarctic Research Expedition. We thank Takuji Nakamura for his many useful comments and discussions. We also thank Arata Amemiya for describing the idealized ray tracing model. Numerical simulations were run on the NIPR supercomputer. All figures shown in this paper were created using the Dennou Club Library (DCL). This study was supported by the Program for Leading Graduate Schools, MEXT, Japan. The study was also supported through the Japan Society for the Promotion of Science (JSPS) Grant-in-Aid Scientific Research (A) 25247075 (Kaoru Sato) and Grant-in-Aid for Research Fellow (26-9257) (Ryosuke Shibuya) programs.

## References

Akmaev, R. A., J. M. Forbes, F.-J. Lübken, D. J. Murphy, and J. Höffner, 2016: Tides in the mesopause region over Antarctica: Comparison of whole atmosphere model simulations with ground-based observations, *J. Geophys. Res. Atmos.*, **121**, 1156–1169, doi:10.1002/2015JD023673.

Alexander, M. J., M. Geller, C. McLandress, S. Polavarapu, P. Preusse, F. Sassi, K. Sato, S. Eckermann, M. Ern, A. Hertzog, Y. Kawatani, M. Pulido, T. Shaw, M. Sigmond, R. Vincent, S. Watanabe, 2010: Recent developments in gravity wave effects in climate models, and the global distribution of gravity wave momentum flux from observations and models, *Q. J. Roy. Meteorol. Soc.*, **136**, 1103-1124.

Aso, T., 2007: A note on the semidiurnal non-migrating tide at polar latitudes, *Earth Planets Space*, **59**, e21–e24.

Baldwin, M. P., and Coauthors, 2003: The Quasi-Biennial Oscillation, *Rev. Geophys.*, **39,** 179-229.

Becker, E., 2009: Sensitivity of the upper mesosphere to the Lorenz energy cycle of the

troposphere, *J. Atmos. Sci.*, **66**, 647–666, doi: 10.1175/2008JAS2735.1.

Bloom, S., L. Takacs, A. DaSilva, and D. Ledvina, 1996: Data assimilation using incremental analysis updates. *Mon. Wea. Rev.*, **124**, 1256–1271.

Bühler, O., and M. E. McIntyre, 2005: Wave capture and wave-vortex duality. *J. Fluid. Mech.,* **534,** 67-95.

Chen, C., X. Chu, A. J. McDonald, S. L. Vadas, Z. Yu, W. Fong, and X. Lu, 2013: Inertia‐gravity waves in Antarctica: A case study using simultaneous lidar and radar measurements at McMurdo/Scott Base (77.8° S, 166.7° E). *Journal of Geophysical Research: Atmospheres*, **118**(7), 2794-2808.

Cherniak I and I. Zakharenkova, 2016: High-latitude ionospheric irregularities: differences between ground- and space-based GPS measurements during the 2015 St. Patrick's Day Storm. Earth Planets Space 68:136. doi:10.1186/s40623-016-0506-1

Chu, X., W. Huang, F. Fong, Z. Yu, Z. Wang, J. A. Smith, and C. S. Gardner 2011: First lidar observations of polar mesospheric clouds and Fe temperatures at McMurdo (77.8°S, 166.7°E), Antarctica, *Geophys. Res. Lett.*, **38**, L16810, doi:10.1029/2011GL048373.

Collins, R. L., D. C. Senft, and C. S. Gardner 1992: Observations of a 12 H wave in the mesopause region at the South Pole, *Geophys. Res. Lett.*, **19**(1), 57–60, doi:10.1029/91GL02780.

Eyring, V., T. G. Shepherd, and D. W. Waugh, Eds., 2010: SPARC CCMVal report on the evaluation of chemistry-climate models. SPARC Rep. 5, WCRP-132, WMO/TD-No. 1526, 434 pp.

Fisher, G. M., R. J, Niciejewski, T. L. Killeen, W. A. Gault, G. G. Shepherd, S. Brown, and Q. Wu, 2002: Twelve‐hour tides in the winter northern polar mesosphere and lower thermosphere. *Journal of Geophysical Research: Space Physics*, **107**(A8).

Fraser, G. J. and U. Khan, 1990: Semidiurnal variations in the time scale of irregularities near

the Antarctic summer mesopause. *Radio science*, **25**(5), 997-1003.

Forbes, J. M., N. A. Makarov, and Y. I. Portnyagin, First results from the meteor radar at south pole: A large 12-hour oscillation with zonal wavenumber one, *Geophys. Res. Lett.,* **22,** 3247– 3250, 1995.Forbes, J.M.,

Forbes, J. M., Y. I. Portnyagin, N. A. Markov, S. E. Palo, E. G. Merzlyakov and X. Zhang, 1999: Dynamics of the lower thermosphere over South Pole from meteor radar windmeasurements. *Earth Planets Space,* **51**, 611–620.

Fritts, D. C., D. M. Riggin, B. B. Balsley, and R. G. Stockwell 1998: Recent results with an MF radar at McMurdo, Antarctica: Characteristics and variability of motions near 12-hour period in the mesosphere, *Geophys. Res. Lett.*, **25**(3), 297–300, doi:10.1029/97GL03702.

Fritts , D. C. and M. J. Alexander, 2003: Gravity wave dynamics and effects in the middle atmosphere. *Rev. Geophys.*, **41**, 1003, doi:10.1029/2001RG000106.

Geller, M. A. and J. Gong, 2010: Gravity wave kinetic, potential, and vertical fluctuation energies as indicators of different frequency gravity waves. *Journal of Geophysical Research: Atmospheres*, **115**(D11).

Geller, M. A., M. Alexander, P. T. Love, J. Bacmeister, M. Ern, A. Hertzog, T. Zhou, 2013: A Comparison between Gravity Wave Momentum Fluxes in Observations and Climate Models. *Journal of Climate*, **26**(17).

Guest, F. M., M. J. Reeder, C. J. Marks, and D. J. Karoly (2000), Inertia-gravity waves observed in the lower stratosphere over Macquarie Island, *J. Atmos. Sci.*, **57**, 737–752.

Hagan, M. E., and J. M. Forbes, 2003: Migrating and nonmigrating semidiurnal tides in the upper atmosphere excited by tropospheric latent heat release, *J. Geophys. Res.,* **108(A2),** 1062, doi:10.1029/2002JA009466.

Haynes, P. H., 1998: The latitudinal structure of the quasi-biennial oscillation. *Quart. J. Roy.*

*Meteor. Soc.,* **124,** 2645-2670.

Hernandez, G., G. J. Fraser, and R. W. Smith 1993: Mesospheric 12-hour oscillation near South Pole, Antarctica, *Geophys. Res. Lett.*, **20**(17), 1787–1790, doi:10.1029/93GL01983.

Hertzog, A., G. Boccara, R. A. Vincent, F. Vial, and P. Cocquerez, 2008: Estimation of gravity wave momentum flux and phase speeds from quasi-Lagrangian stratospheric balloon flights. Part II: Results from the Vorcore campaign in Antarctica. *Journal of the Atmospheric Sciences*, **65**(10), 3056-3070.

Hirota, I. and T. Niki, 1986: Inertia-gravity waves in the troposphere and stratosphere observed by the MU radar. *J. Meteor. Soc. Japan,* **64**, 995−999.

Jacobsen, K. S., and M. Dähnn (2014), Statistics of ionospheric disturbances and their correlation with GNSS 338 positioning errors at high latitudes, *J. Space Weather Space Clim.*, **4**, A27, doi:10.1051/swsc/2014024.

Kataoka, R., D. Shiota, E. Kilpua, and K. Keika 2015: Pileup accident hypothesis of magnetic storm on 17 March 2015, *Geophys. Res. Lett.*, **42**, 5155–5161, doi:10.1002/2015GL064816.

Kohma, M. and K. Sato, 2011: The effects of atmospheric waves on the amounts of polar stratospheric clouds. *Atmos. Chem. Phys.,* **11**, 11535-11552, doi:10.5194/acp-11-11535-2011.

Lane, T. P., J. D. Doyle, R. Plougonven, M. A. Shapiro, and R. D. Sharman, 2004: Observations and numerical simulations of inertia-gravity waves and shearing instabilities in the vicinity of a jet stream. *J. Atmos. Sci.,* **61,** 2792-2706.

Li, T., C.-Y. She, H.-L. Liu, T. Leblanc, and I. S. McDermid, 2007: Sodium lidar–observed strong inertia-gravity wave activities in the mesopause region over Fort Collins, Colorado (41°N, 105°W), *J. Geophys. Res.*, **112**, D22104, doi:10.1029/2007JD008681.

Liu, H. L., J. M. McInerney, S. Santos, P. H. Lauritzen, M. A. Taylor, and N. M. Pedatella, 2014: Gravity waves simulated by high‐resolution Whole Atmosphere Community Climate Model. *Geophysical Research Letters*, **41(24)**, 9106-9112.

Lu, X., A. Z. Liu, G. R. Swenson, T. Li, T. Leblanc, and I. S. McDermid, 2009: Gravity wave propagation and dissipation from the stratosphere to the lower thermosphere, *J. Geophys. Res.*, **114**, D11101, doi:10.1029/2008JD010112.

Marks, C. J., and S. D. Eckermann, 1995: A three-dimensional nonhydrostatic ray tracing model for gravity waves: Formulation and preliminary results for the middle atmosphere. *J. Atmos. Sci.*, **52**(11), 1959-1984.

Mayr, H. G., J. G. Mengel, E. R. Talaat, H. S. Porter, and K. L. Chan, 2005a: Mesospheric non-migrating tides generated with planetary waves: I. Characteristics, *J. Atmos. Sol. Terr. Phys.,* **67**, 959– 980.

Mayr, H. G., J. G. Mengel, E. R. Talaat, H. S. Porter, and K. L. Chan, 2005b: Mesospheric non-migrating tides generated with planetary waves: II. Influence of gravity waves, *J. Atmos. Sol. Terr. Phys.,* **67**, 981–991.

McDonald, A. J., S. E. George, and R. M. Woollands, 2009: Can gravity waves significantly impact PSC occurrence in the Antarctic?, *Atmos. Chem. Phys.*, **9**, 8825–8840, doi:10.5194/acp-9-8825-2009.

McLandress, C., T. G. Shepherd, S. Polavarau, S. R. Beagley, 2012: Is Missing Orographic Gravity Wave Drag near 60°S the Cause of the Stratospheric Zonal Wind Biases in Chemistry–Climate Models?. *J. Atmos. Sci.,* **69**, 802–818, 2012.

McFarlane, N. A., 1987: The effect of orographically excited wave drag on the general circulation of the lower stratosphere and troposphere. *J. Atmos. Sci.*, **44**, 1775–1800.

Mihalikova, M., Sato, K., Tsutsumi, M., and Sato, T, 2016.: Properties of inertia-gravity waves in the lowermost stratosphere as observed by the PANSY radar over Syowa

Station in the Antarctic, Ann. Geophys., 34, 543-555, doi:10.5194/angeo-34-543-2016.

Moffat-Griffin, T., M. J. Jarvis, S. R. Colwell, A. J. Kavanagh, G. L. Manney, and W. H. Daffer (2013), Seasonal variations in the lower stratospheric gravity wave energy above the Falkland Islands, *J. Geophys. Res. Atmos.*, **118**, 10,861–10,869, doi:10.1002/jgrd.50859.

Murphy, D. J., et al., 2006: A climatology of tides in the Antarctic mesosphere and lower thermosphere, *J. Geophys. Res.*, **111**, doi:10.1029/2005JD006803.

Murphy, D. J., T. Aso, D. C. Fritts, R. E. Hibbins, A. J. McDonald, D. M. Riggin, M. Tsutsumi, and R. A. Vincent, 2009: Source regions for Antarctic MLT non-migrating semidiurnal tides, *Geophys. Res. Lett.*, **36**, L09805, doi:10.1029/2008GL037064.

Murphy, D. J., S. P. Alexander, A. R. Klekociuk, P. T. Love, and R. A. Vincent, 2014: Radiosonde observations of gravity waves in the lower stratosphere over Davis, Antarctica. J. Geophys. Res. Atmos., 119, 11 973–11 996, doi:10.1002/ 2014JD022448.

Nakamura, T., T. Tsuda, M. Yamamoto, S. Fukao, and S. Kato 1993: Characteristics of gravity waves in the mesosphere observed with the middle and upper atmosphere radar 2. Propagation direction, *J. Geophys. Res.*, **98**(D5), 8911–8923, doi:10.1029/92JD03030.

Nakanishi M. and H. Niino, 2004: An Improved Mellor–Yamada Level-3 Model with Condensation Physics: Its Design and Verification. *Boundary-Layer Meteorol.* **112**,1–31

Nastrom, G. D., and F. D. Eaton 2006: Quasi-monochromatic inertiagravity waves in the lower stratosphere from MST radar observations, *J. Geophys. Res.*, **111**, D19103, doi:10.1029/2006JD007335.

Nicolls, M. J., R. H. Varney, S. L. Vadas, P. A. Stamus, C. J. Heinselman, R. B. Cosgrove, and M. C. Kelley 201:, Influence of an inertia-gravity wave on mesospheric dynamics: A case study with the Poker Flat Incoherent Scatter Radar, *J. Geophys. Res.*, **115**, D00N02, doi:10.1029/2010JD014042.

1  Okamoto, K., K. Sato, and H. Akiyoshi, 2011: A study on the formation and trend of the

2      Brewer-Dobson circulation. *J. Geophys. Res.*, **116,** D10117, doi:10.1029/2010JD014953.

3  O'Sullivan, D. J., and T. J. Dunkerton, 1995: Generation of inertia-gravity waves in a

4      simulated life cycle of baroclinic instability. *J. Atmos. Sci.,* **52,** 3695-3716.

5  Pavelin, E. G., J. A. Whiteway, and G. Vaughan, Observation of gravity wave generation and

6      breaking in the lowermost stratosphere, 2001: *J. Geophys. Re*s., **106**, 5173 – 5179.

7  R. Plougonven and C. Snyder, 2007: Inertia-gravity waves spontaneously generated by jets

8      and fronts. Part I: Different baroclinic life cycles. *J. Atmos. Sci.*, **64**, p2502-2520.

9  Plumb, R. A., 2002: Stratospheric transport. *J. Meteor. Soc. Japan,* **80,** 793-809.

10  Portnyagin, Y. I., J. M. Forbes, N. A. Makarov, E. G. Merzlyakov, and S.Palo, The

11      summertime 12-h wind oscillation with zonal wavenumber s =1 in the lower

12      thermosphere over the South Pole, *Ann. Geophys.*, **16**,828– 837, 1998.

13  Reid, I. M., and R. A. Vincent, 1987: Measurements ofmesospheric gravity wave momentum

14      fluxes and mean flow accelerations at Adelaide, Australia, *J. Atmos. Terrest. Phys*. **49**,

15      443-460.

16  Richter, J. H., F. Sassi, and R. R. Garcia, 2009: Toward a physically based gravity wave

17      source parameterization in a general circulation model, *J. Atmos. Sci.,* **67**, 136–156.

18  Rienecker, M., and Coauthors, 2011: MERRA: NASA's ModernEra Retrospective Analysis

19      for Research and Applications. *J. Climate*, **24**, 3648–3624.

20  Riggin, D. M., D. C. Fritts, M. J. Jarvis, G. O. L. Jones, 1999: Spatial structure of the 12-hour

21      wave in the Antarctic as observed by radar. *Earth Planets and Space*, **51**, 621–628.

22  Sato, K., 1994: A statistical study of the structure, saturation and sources of inertio-gravity

23      waves in the lower stratosphere observed with the MU radar.

24      *J. Atmos. Terr. Phys.,* **56,** 755-774.

25  Sato, K., T. Kinoshita, and K. Okamoto, 2013: A new method to estimate three-dimensional

residual mean circulation in the middle atmosphere and its application to gravity-wave

resolving general circulation model data, *J. Atmos. Sci.*, **70**, 3756–3779.

doi: http://dx.doi.org/10.1175/JAS-D-12-0352.1.

Sato, K., D. J. O'Sullivan, and T. J. Dunkerton, 1997: Low-frequency inertia-gravity waves in

the stratosphere revealed by three-weak continuous observation with the MU radar.

*Geophys. Res. Lett.*, **24,** 1739-1742.

Sato, K., and T. J. Dunkerton, 1997: Estimates of momentum flux associated with equatorial

Kelvin and gravity waves. *J. Geophys. Res.,* **102**, 26,247-26,261.

Sato, K., M. Tsutsumi, T. Sato, T. Nakamura, A. Saito, Y. Tomikawa, K. Nishimura, M.

Kohma, H. Yamagishi, and T. Yamanouchi, 2014: Program of the Antarctic Syowa

MST/IS Radar (PANSY), *J. Atmos. Solar-Terr. Phys*., **118A**, 2-15, 2014.

Sato, K., S. Watanabe, Y. Kawatani, Y. Tomikawa, K. Miyazaki, and M. Takahashi, 2009:

On the origins of mesospheric gravity waves, *Geophys. Res. Lett.,* **36,** L19801,

doi:10.1029/2009GL039908.

Sato, K., S. Tateno S. Watanabe, and Y. Kawatani (2012), Gravity wave characteristics in the

Southern Hemisphere revealed by a high-resolution middle-atmosphere general

circulation model. *J. Atmos. Sci.*, **69**, 1378–1396, doi:10.1175/JAS-D-11-0101.1.

Sato, K., and M. Yoshiki, 2008: Gravity wave generation around the polar vortex in the

stratosphere revealed y 3-houly radiosonde observations at Syowa Station. *J. Atmos.*

*Sci.,* **65,** 3719-3735.

Sato, K., and M. Yamada, 1994: Vertical structure of atmospheric gravity waves revealed by

the wavelet analysis. *Journal of Geophysical Research: Atmospheres (1984–*

*2012)*, **99**(D10), 20623-20631.

Kaoru Sato, Masashi Kohma, Masaki Tsutsumi, and Toru Sato, 2017: Frequency spectra and

vertical profiles of wind fluctuations in the summer Antarctic mesosphere revealed by

MST radar observations. *Journal of Geophysical Research: Atmospheres* **122**:1, 3-19.

Satoh, M., T. Matsuno, H. Tomita, H. Miura, T. Nasuno, and S. Iga, 2008: Nonhydrostatic icosahedral atmospheric model (NICAM) for global cloud resolving simulations. *J. Comput. Phys.*, the special issue of Predicting Weather, Climate and Extreme Events, **227**, 3486−3514, doi: 10.1016/j.jcp.2007.02.006.

Satoh, M., Tomita, H., Yashiro, H., Miura, H., Kodama, C., Seiki, T., Noda, A. T., Yamada, Y., Goto, D., Sawada, M., Miyoshi, T., Niwa, Y., Hara, M., Ohno, T., Iga, S., Arakawa, T., Inoue, T., Kubokawa, H., 2014: The Non-hydrostatic Icosahedral Atmospheric Model: Description and Development. *Progress in Earth and Planetary Science,* 1, **18**. doi:10.1186/s40645-014-0018-1

Scinocca, J. F., 2003: An accurate spectral nonorographic gravity wave drag parameterization for general circulation models. *J. Atmos. Sci.,* **60,** 667-682.

Shibata, T., K. Sato, H. Kobayashi, M. Yabuki, and M. Shiobara, 2003: The Antarctic polar stratospheric clouds under the temperature perturbation by nonorogaphic inertia-gravity waves observed by micropulse lidar. *J. Geophys. Res.,* **108**, 4105, doi:10.1029/2002JD002713.

Shibuya R., H. Miura and K. Sato, 2016: A grid transformation method for a quasi-uniform, circular fine region using the spring dynamic, *Journal of the Meteorological Society of Japan*, 94, doi:10.2151/jmsj.2016-022.

Shibuya, R., K. Sato, Y. Tomikawa, M. Tsutsumi and T. Sato, 2015: A study of multiple tropopause structures caused by inertia-gravity waves in the Antarctica, *J. Atmos. Sci.*, **72**, 2109–2130.

Stolarski, R. S., A. R. Douglass, M. Gupta, P. A. Newman, S. Pawson, M. R. Schoeberl, and J. E. Nielsen, 2006: An ozone increase in the Antarctic summer stratosphere: A

dynamical response to the ozone hole. *Geophys. Res. Lett.,* **33,** L21805, doi:10.1029/2006GL026820.

Talaat, E. R., and H.G. Mayr, 2011: Model of semidiurnal pseudo tide in the high-latitude upper mesosphere, *Journal of Atmospheric and Solar-Terrestrial Physics,* **73**, 2386–2391

Tomita, H., M. Satoh, K. Goto, 2002: An optimization of icosahedral grid by using spring dynamics. *J. Comp. Phys.*, **183**, 307-331.

Vaughan, G., and R. M. Worthington 2007: Inertia-gravity waves observed by the UK MST radar, *Q. J. R. Meteorol. Soc.*, **133**: (S2) 179–188.

Vincent, R. A., I. M. Reid, 1983: HF Doppler Measurements of Mesospheric Gravity Wave Momentum Fluxes. *J. Atmos. Sci.*, **40**, 1321–1333. doi: 10.1175/1520-0469(1983)040<1321:HDMOMG>2.0.CO;2

Walterscheid, R. L., G. G. Sivjee, G. Schubert and R. M. Hamwey, 1986: Large-amplitude semidiurnal temperature variations in the polar mesopause: evidence of a pseudotide. *Nature*, **324**(6095), 347-349.

Wang, L., M. A. Geller, and M. J. Alexander 2005: Spatial and temporal variations of gravity wave parameters. Part I: Intrinsic frequency, wavelength, and vertical propagation direction, *J. Clim.*, **62,** 125–142.

Watanabe, S., K. Sato, and M. Takahashi, 2006: A general circulation model study of the orographic gravity waves over Antarctica excited by katabatic winds. *J. Geophys. Res.,* **111**, D18104, doi:10.1029/2005JD006851.

Watanabe, S., K. Sato, Y, Kawatani, and M. Takahashi, 2015: Vertical resolution dependence of gravity wave momentum flux simulated by an atmospheric general circulation model, *Geosci. Model Dev.,* **8,** 1637-1644, doi:10.5194/gmd-8-1637-2015.

Wu, W.-S., R. J. Purser, and D. F. Parrish, 2002: Three-dimensional variational analysis with spatially inhomogeneous covariances. *Mon. Wea. Rev.*, **130,** 2905–2916.

Wu, Q., Killeen, T. L., Nozawa, S., McEwen, D., Guo, W., & Solomon, S. C. (2003).
    Observations of mesospheric neutral wind 12-hour wave in the Northern Polar
    Cap. *Journal of atmospheric and solar-terrestrial physics*, **65**(8), 971-978.

Yamashita, K., S. Miyahara, Y. Miyoshi, K. Kawano, and J. Ninomiya, Seasonal variation of
    non-migrating semidiurnal tide in the polar MLT region in a general circulation model,
    *J. Atmos. Solar-Terr. Phys.*, **64**, 1083–1094, 2002.

Yasuda, Y., K. Sato, and N. Sugimoto, 2015: A Theoretical Study on the Spontaneous
    Radiation of Inertia-gravity Waves Using the Renormalization Group Method. Part I:
    Derivation of the Renormalization Group Equations,
    *J. Atmos. Sci.*, **72**, 957–983, doi:10.1175/JAS-D-13-0370.1

Yasuda, Y., K. Sato, and N. Sugimoto, 2015: A Theoretical Study on the Spontaneous
    Radiation of Inertia-gravity Waves Using the Renormalization Group Method. Part II:
    Verification of the Theoretical Equations by Numerical Simulation,
    *J. Atmos. Sci.*, **72**, 984–1009, doi:10.1175/JAS-D-13-0371.1

Yasui, R., K. Sato and M. Tsutsumi, 2016: Seasonal and interannual variation of mesospheric
    gravity waves based on MF radar observations over 15 years at Syowa Station in the
    Antarctic., *SOLA*, **12**, 46-50, doi:10.2151/sola.2016-010.

Yoshiki, M., and K. Sato (2000), A statistical study of gravity waves in the polar regions
    based on operational radiosonde data, *J. Geophys. Res.*, **105**(D14), 17,995–18,011.

Zhang, F., S. E. Koch, C. A. Davis, and M. L. Kaplan, 2001: Wavelet analysis and the
    governing dynamics of a large-amplitude mesoscale gravity-wave event along the East
    Coast of the United States. *Quart. J. Roy. Meteor. Soc.,* **127,** 2209-2245.

**Table and Figure captions**

- Table 1: The wave parameters of fluctuations in the mesosphere observed over Syowa
    Station (a) obtained by fitting to a sinusoidal function using a nonlinear least square

1     method (b) estimated on the hypothesis that fluctuations are due to inertia-gravity waves,

2     where $\alpha$ is the angle of $u_{\parallel}$ measured clockwise from the east.

3 ● Table 2: The directly estimated wave parameters of packets simulated over Syowa

4     Station

5 ● Table 3: The results of the idealized ray tracing and the manual wave packet tracing

7 ● Figure 1:   (a) An illustration of the stretched grid (roughened up to glevel-3).   (b) A

8     horizontal map of a normalized grid interval defined as $d/\Delta x$, where $d$ denotes grid

9     intervals and $\Delta x$ denotes the grid interval of the original icosahedral grid.

10 ● Figure 2: Time-altitude cross sections of (a) eastward line of sight velocity components

11     observed by the PANSY radar at Syowa Station for the period from 17 March 2015 to 23

12     March 2015, (b) for the period from 21 March 2015 to 23 March 2015, and (c) opposite

13     of westward line of sight velocity components for the period from 21 March 2015 to 23

14     March 2015. The dashed line in (b) and (c) denotes phase lines with the downward phase

15     velocity of 0.3 m s$^{-1}$. The green arrows in (c) denotes the wave period of the disturbance.

16     The contour intervals are 2 m s$^{-1}$.

17 ● Figure 3: Time-altitude cross sections of (a) zonal wind components and (b) meridional

18     wind components observed by the PANSY radar at Syowa Station for the period from 17

19     March 2015 to 23 March 2015. The contour intervals are 12 m s$^{-1}$.

20 ● Figure 4: Zonal and meridional wind components observed on 23 March 2015 as a

21     function of time at heights of (a) 70.8 km and (b) 72.0 km. Zonal and meridional wind

22     components fitted sinusoidal functions using a nonlinear least squares method at the

23     height of (c) 70.8 km and (d) 72.0 km. The circles denote the zonal wind components and

24     the star marks denote the meridional components.

1 ● Figure 5: A hodograph of the fitted horizontal wind components in the time region from

2 00 UTC 23 to 13 UTC 23 March at the height of (a) 70.8 km and (b) 72.0 km from the

3 PANSY radar observation. Each mark is plotted at one hour interval.

4 ● Figure 6: Time-altitude cross sections of (a) eastward line-of-sight velocity components

5 simulated by NICAM at Syowa Station (contour interval 2 m s$^{-1}$) for the period from 17

6 March 2015 to 23 March 2015, (b) for the period from 21 March 2015 to 23 March 2015

7 (contour interval 3 m s$^{-1}$). (c) Zonal wind components in eastward line-of-sight velocity

8 components for the period from 21 March 2015 to 23 March 2015 (contour interval 18 m

9 s$^{-1}$).

10 ● Figure 7: Time-altitude cross sections of (a) anomalies of the zonal wind components

11 from the time-mean components, (b) the diurnal and semi-diurnal migrating tidal

12 components, (c) the planetary wave components, (d) small-scale gravity waves and (e)

13 the remaining components. The contour intervals are 10 m s$^{-1}$.

14 ● Figure 8: Time-altitude cross sections of the envelope function of the zonal wind

15 components of the large-scale gravity waves (contour interval 10 m s$^{-1}$) .The figure from

16 (i) to (v) denote the labels of the wave packet examined in Section 4.

17 ● Figure 9: A hovmöller diagram of zonal wind components of the large-scale inertia-

18 gravity waves at the height of 70 km at 69°S (contour interval 10 m s$^{-1}$). The figures (i),

19 (ii) and (v) indicate the packets labeled in Fig.5.

20 ● Figure 10: A composite map of zonal wind components of the large-scale inertia-gravity

21 waves. The height where the composites are taken and the reference time is (a) 70 km, 06

22 UTC 19 March, (b) 70 km, 15 UTC 20 March, (c) 75 km, 15 UTC 21 March, (d) 65 km,

23 03 UTC 22 March and (e) 72 km,14 UTC 22 March. The contour intervals are 10 m s$^{-1}$.

24 ● Figure 11: Snapshots of the zonal wind components and their envelope function of the

25 large-scale inertia-gravity waves (a) at the height of 70 km at 03 UTC 23 March 2015,

1    corresponding to the packet (v), and (c) at the height of 70 km at 01 UTC 19 March

2    2015, corresponding to the packet (i). Hovmöller diagrams of the zonal wind components

3    and their envelope function of the large-scale inertia-gravity waves at the height of 70 km

4    at 69°S for the period (b) from 20 to 23 March and (d) from 17 to 20 March. The green

5    dashed curves in (a) and (c) denote the cross section taken in (b) and (d), and vice versa.

6    The green circles are locations of traced wave packets by the method discussed in the

7    text. The contour intervals are 10 m s$^{-1}$.

8    ● Figure 12: Snapshots of the zonal wind components of the large-scale inertia-gravity

9    waves tracing the packet (v) (a) at the height of 60 km at 23 UTC 22 March (contour

10    interval 10 m s$^{-1}$), (b) at the height of 40 km at 08 UTC 22 March (contour interval 5 m

11    s$^{-1}$), (c) at the height of 25 km at 16 UTC 21 March (contour interval 3 m s$^{-1}$) and (d) at

12    the height of 23 km at 03 UTC 21 March (contour interval 2 m s$^{-1}$). Snapshots for the

13    packet (i) (e) at the height of 63 km at 23 UTC 22 March, (f) at the height of 58 km at 15

14    UTC 18 March, (g) at the height of 53 km at 11 UTC 18 March (contour interval 5 m s$^{-}$

15    $^{1}$), (d) at the height of 48 km at 08 UTC 18 March (contour interval 3 m s$^{-1}$). The green

16    circles are locations of traced wave packets by the method discussed in the text.

17    ● Figure 13: The ray path of (a, b) the packet (v) and (c, d) the packet (i) using the

18    idealized ray tracing method (black thick line, colored circles) and the manual wave

19    packet tracing method (colored star marks) in (a, c) the latitude-height cross section and

20    (b, d) the horizontal map. The contours in (a, c) denotes background zonal wind

21    components averaged in the zonal direction and for the period from 17 March to 23

22    March.

23    ● Figure 14: A snapshots of longitude-height cross sections of zonal wind components of

24    the large-scale inertia-gravity waves (above the height of 19 km, the left color bar,

25    contour interval 2 m s$^{-1}$) and the absolute values of the horizontal wind components

1     (below the height of 18 km, the right color bar, contour interval 10 m s$^{-1}$) at 03 UTC 21

2     March at 40°S.

3  ● Figure 15: Snapshots of horizontal maps of (a) the absolute horizontal wind velocity and

4     (b) the residual of the nonlinear balance equation ($\Delta NBE$) at the height of 10 km at 03

5     UTC 21 March 2015. The vectors in (a) denote the directions and the magnitude of the

6     horizontal winds. The contour intervals in (a) are 10 m s$^{-1}$.

7  ● Figure 16: (a) A longitude-height cross section of zonal wind components of the large-

8     scale inertia-gravity waves $\sqrt{\rho_0}u'$ at 69°S at 15 UTC 18 March (contour interval 0.1

9     Pa$^{0.5}$), and (b) a line plot of the energy flux $\overline{p'w'}$ averaged from the longitude of -90°E to

10    the longitude of 60°E. The thick black contours show background zonal wind components

11    extracted by a lowpass filter with a cutoff wavelength of 4000 km. The thick contours

12    denote 20 m s$^{-1}$, 30 m s$^{-1}$ and 40 m s$^{-1}$, respectively.

13 ● Figure 17: Latitude-height cross sections of (a) the vertical fluxes of zonal momentum

14    $\rho_0\overline{u'w'}$, (b) the vertical fluxes of zonal momentum $\rho_0\overline{v'w'}$, (c) the ratio of the Coriolis

15    parameter to the intrinsic frequency $f/\widehat{\omega}$, (d) the kinetic energies of the horizontal wind

16    components and (e) the potential energies of the large-scale inertia-gravity waves, which

17    are averaged in the zonal direction and for the period from 19 March to 21 March 2015.

18    The contour interval is (a, b) $2.0 \times 10^{-5}$ [Pa], (c) 0.1, respectively. It should be noted

19    that the color bar and the contour interval in (d) and (e) are log-scaled.

Table 1: The wave parameters of fluctuations in the mesosphere observed over Syowa Station (a) obtained by fitting to a sinusoidal function using a nonlinear least square method (b) estimated on the hypothesis that fluctuations are due to inertia-gravity waves, where $\alpha$ is the angle of $u_\parallel$ measured clockwise from the east. The error bar is based on the uncertainty by using a nonlinear least square method.

Table 1a

| Time and height locations | $\omega$ (s$^{-1}$) | $m$ (m$^{-1}$) from $u'$ | $C_{p_z}$(m s$^{-1}$) from $u'$ | $m$ (m$^{-1}$) from $v'$ | $C_{p_z}$(m s$^{-1}$) from $v'$ |
|---|---|---|---|---|---|
| 3/22 73.2 km | $1.42 \times 10^{-4}$ (12.3 h) | | | | |
| 3/22 73.8 km | $1.27 \times 10^{-4}$ (13.7 h) | $5.24 \times 10^{-4}$ (12.0 km) | $-0.26$ | $7.42 \times 10^{-4}$ (8.47 km) | $-0.19$ |
| 3/22 74.4 km | $1.59 \times 10^{-4}$ (11.0 h) | | | | |
| 3/23 70.8 km | $1.35 \times 10^{-4}$ (12.9 h) | | | | |
| 3/23 71.4 km | $1.35 \times 10^{-4}$ (12.9 h) | $4.08 \times 10^{-4}$ (15.4 km) | $-0.34$ | $5.11 \times 10^{-4}$ (12.3 km) | $-0.28$ |
| 3/23 72.0 km | $1.42 \times 10^{-4}$ (12.3 h) | | | | |

Table 1b

| Time and height locations | $u'$ (m s$^{-1}$) | $v'$ (m s$^{-1}$) | $\|2\pi/k_h\|$ (km) | $\alpha$ (degree) | $\dfrac{f}{\widehat{\omega}}$ |
|---|---|---|---|---|---|
| 3/22 73.2 km | 28.5 $\pm$ 2.8 | 21.3 $\pm$ 2.8 | 1775 (1207 ~ 2797) | 12° (7° ~ 32°) | 0.72 (0.57 ~ 0.85) |
| 3/22 73.8 km | 30.3 $\pm$ 4.5 | 27.0 $\pm$ 4.5 | 3238 (1577 ~ 3407) | 18° (5° ~ 77°) | 0.86 (0.63 ~ 0.87) |
| 3/22 74.4 km | 28.3 $\pm$ 5.9 | 29.3 $\pm$ 5.9 | 1790 (1118 ~ 1793) | 48° (17° ~ 75°) | 0.76 (0.59 ~ 0.76) |
| 3/23 70.8 km | 32.2 $\pm$ 4.8 | 22.8 $\pm$ 4.8 | 1785 (990 ~ 7778) | 2° (1° ~ 52°) | 0.56 (0.41 ~ 0.97) |
| 3/23 71.4 km | 28.7 $\pm$ 6.1 | 22.1 $\pm$ 6.1 | 1454 (870 ~ 1523) | 14° (11° ~ 61°) | 0.63 (0.41 ~ 0.65) |
| 3/23 72.0 km | 39.0 $\pm$ 8.0 | 23.8 $\pm$ 8.0 | 1150 (570~ 1914) | 14° (10° ~ 47°) | 0.70 (0.32 ~ 0.74) |

Table 2: The directly estimated wave parameters of simulated packets

| Wave packets | $k$ (m⁻¹) | $l$ (m⁻¹) | $m$ (m⁻¹) | $\omega$ (s⁻¹) | $C_{p_x}$ (m s⁻¹) | $C_{p_z}$ (m s⁻¹) | $\dfrac{f}{\widehat{\omega}}$ |
|---|---|---|---|---|---|---|---|
| | — $|k_h|$ (m⁻¹) | | | | | | |
| (i) z = 70 km 3/18 12 UTC ~ 3/19 24 UTC | $-2.48 \times 10^{-6}$ (2530 km) | ~ 0 | $3.96 \times 10^{-4}$ (15.8 km) | $1.42 \times 10^{-4}$ (12.3 h) | $-57.3$ | $-0.36$ | 0.763 |
| | $2.48 \times 10^{-6}$ (2530 km) | | | | | | |
| (ii) z = 70 km 3/20 05 UTC ~ 3/21 01 UTC | $-3.18 \times 10^{-6}$ (1980 km) | $-0.98 \times 10^{-6}$ (6440 km) | $4.10 \times 10^{-4}$ (15.3 km) | $1.47 \times 10^{-4}$ (11.8 h) | $-4.62$ | $-0.36$ | 0.704 |
| | $3.33 \times 10^{-6}$ (1887 km) | | | | | | |
| (iii) z = 75 km 3/21 03UTC ~ 3/22 03 UTC | $-2.79 \times 10^{-6}$ (2250 km) | $-2.48 \times 10^{-6}$ (2530 km) | $3.92 \times 10^{-4}$ (16.0 km) | $1.99 \times 10^{-4}$ (8.8 h) | $-71.3$ | $-0.51$ | 0.617 |
| | $3.73 \times 10^{-6}$ (1685 km) | | | | | | |
| (iv) z = 65 km 3/21 21UTC ~ 3/22 09 UTC | $-3.35 \times 10^{-6}$ (1880 km) | $-2.78 \times 10^{-6}$ (2530 km) | $4.63 \times 10^{-4}$ (13.57 km) | $1.46 \times 10^{-4}$ (11.9 h) | $-43.5$ | $-0.32$ | 0.617 |
| | $4.35 \times 10^{-6}$ (1444 km) | | | | | | |
| (v) z = 72 km 3/22 02 UTC ~ 3/23 02 UTC | $-3.78 \times 10^{-6}$ (1660 km) | $-0.82 \times 10^{-6}$ (7660 km) | $4.52 \times 10^{-4}$ (13.9 km) | $1.59 \times 10^{-4}$ (11.0 h) | $-42.1$ | $-0.35$ | 0.653 |
| | $3.87 \times 10^{-6}$ (1625 km) | | | | | | |

Table 3: The results of the manual wave packet tracing and the ray tracing

| | | Manual wave packet tracing | | | Ray tracing | | |
|---|---|---|---|---|---|---|---|
| | | Longitude[ºE] | Latitude [ºS] | Altitude [km] | Longitude[ºE] | Latitude [ºS] | Altitude [km] |
| Packet (v) | 3/23 03 UTC | 40 | 67 | 70.0 | 40.0 | 67.0 | 70.0 |
| | 3/22 23 UTC | 68 | 66 | 60.0 | 46.2 | 65.6 | 63.9 |
| | 3/22 16 UTC | 75 | 62 | 50.0 | 58.0 | 62.0 | 46.8 |
| | 3/22 08 UTC | 63 | 52 | 40.0 | 71.5 | 57.2 | 33.1 |
| | 3/22 03 UTC | 84 | 53 | 30.0 | 80.8 | 55.4 | 27.0 |
| | 3/21 16 UTC | 80 | 43 | 25.0 | 103.3 | 51.1 | 10.3 |
| | 3/21 03 UTC | 95 | 41 | 23.0 | - | - | - |
| Packet (i) | 3/19 01 UTC | 30 | 70 | 70.0 | 30.0 | 70.0 | 70.0 |
| | 3/18 19 UTC | 32 | 67 | 63.0 | 39.7 | 68.5 | 63.1 |
| | 3/18 15 UTC | 33 | 66 | 58.0 | 47.0 | 66.7 | 56.3 |
| | 3/18 11 UTC | 30 | 62 | 53.0 | 53.5 | 63.7 | 49.7 |
| | 3/18 08 UTC | 30 | 59 | 48.0 | 57.7 | 61.0 | 44.6 |
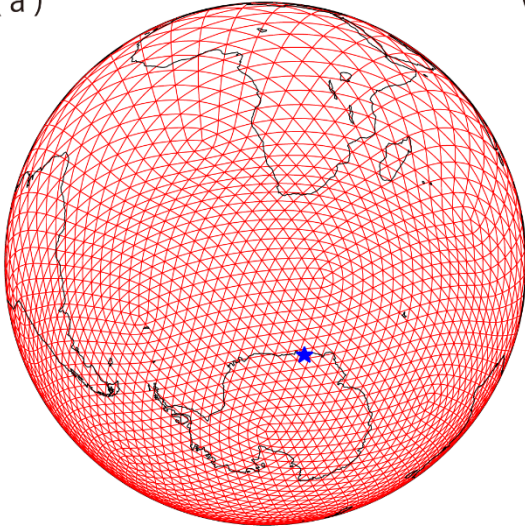
2    Figures

( a )                              ( b )
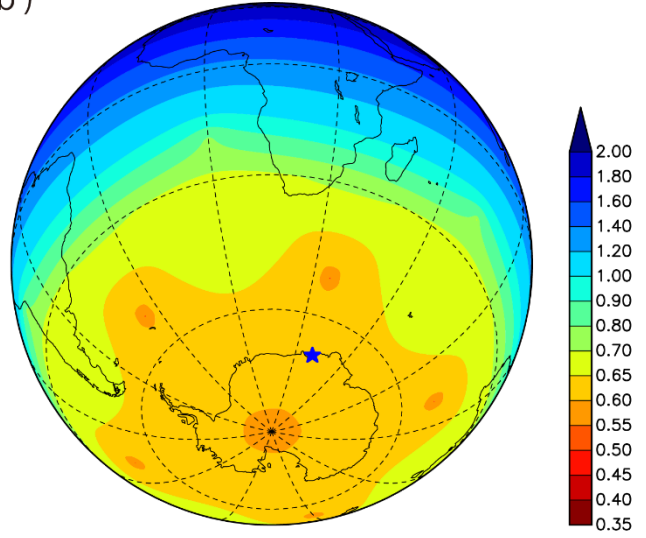
Figure 1:    (a) An illustration of the stretched grid (roughened up to glevel-3).    (b) A horizontal map of a normalized grid interval defined as $d/\Delta x$, where $d$ denotes grid intervals and $\Delta x$ denotes the grid interval of the original icosahedral grid.
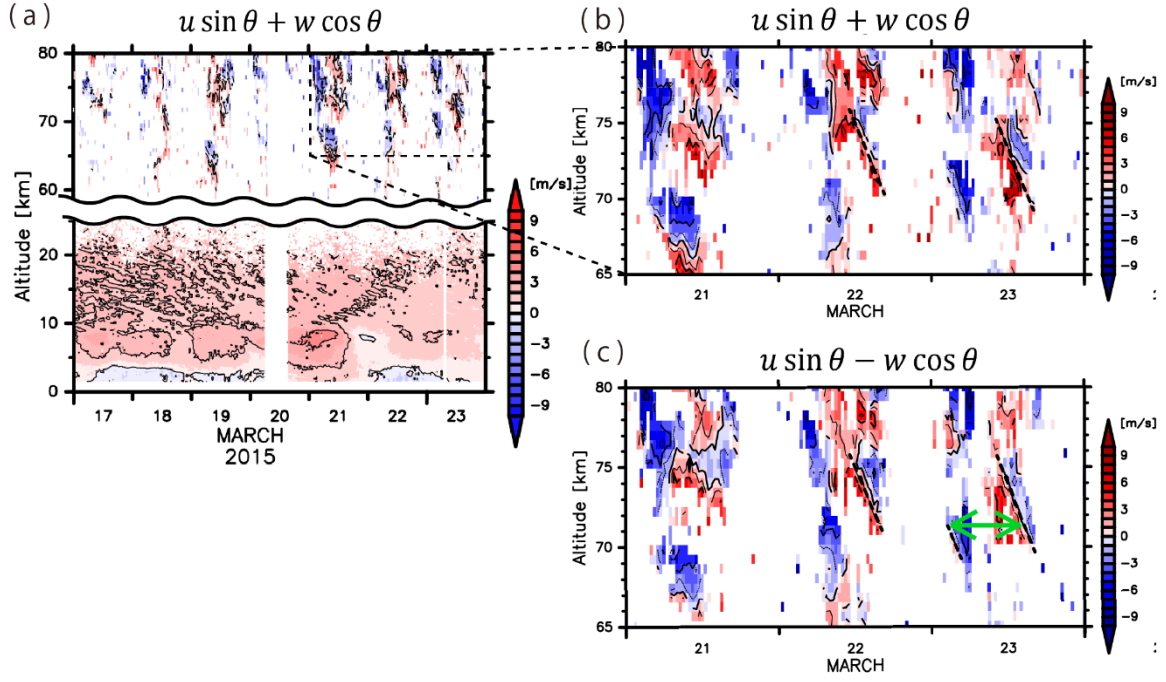
Figure 2: Time-altitude cross sections of (a) eastward line of sight velocity components observed by the PANSY radar at Syowa Station for the period from 17 March 2015 to 23 March 2015, (b) for the period from 21 March 2015 to 23 March 2015, and (c) opposite of westward line of sight velocity components for the period from 21 March 2015 to 23 March 2015. The dashed line in (b) and (c) denotes phase lines with the downward phase velocity of 0.3 m s$^{-1}$. The green arrows in (c) denotes the wave period of the disturbance. The contour intervals are 2 m s$^{-1}$.
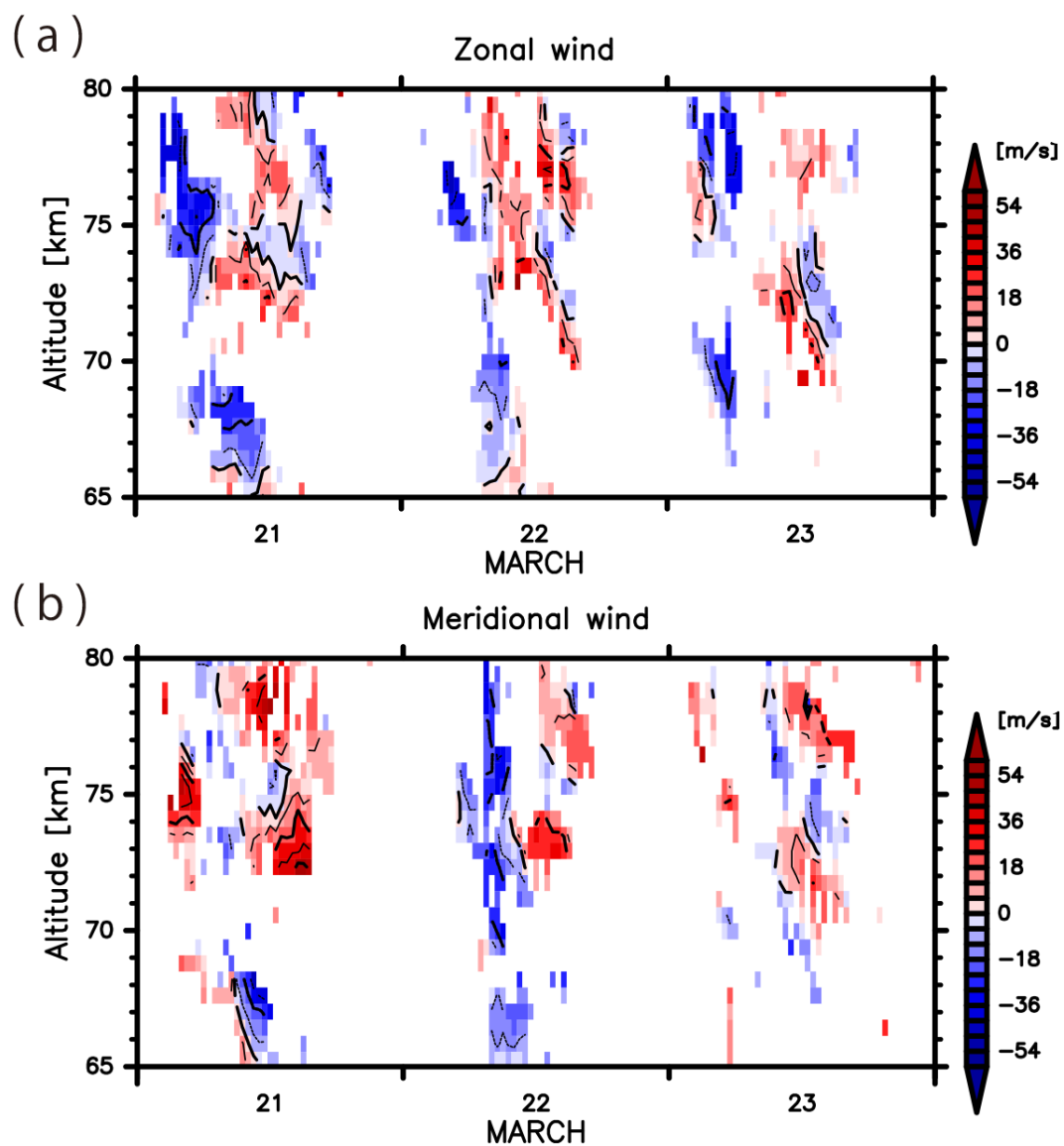
Figure 3: Time-altitude cross sections of (a) zonal wind components and (b) meridional wind components observed by the PANSY radar at Syowa Station for the period from 17 March 2015 to 23 March 2015. The contour intervals are 12 m s$^{-1}$.
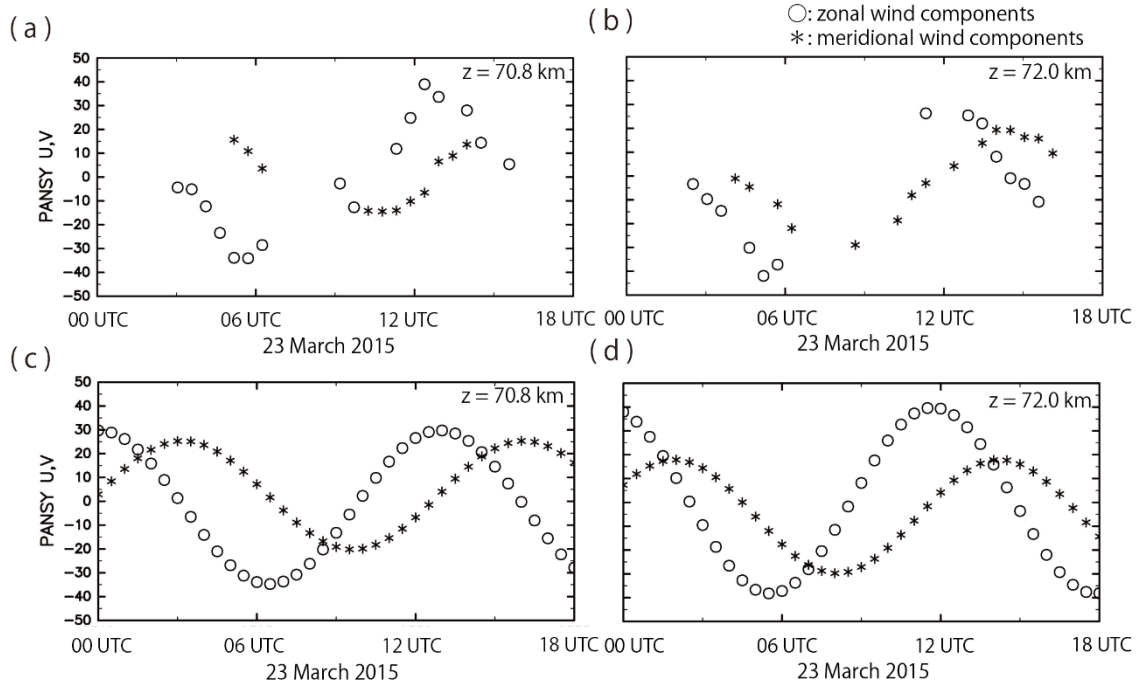
Figure 4: Zonal and meridional wind components observed on 23 March 2015 as a function of time at heights of (a) 70.8 km and (b) 72.0 km. Zonal and meridional wind components fitted sinusoidal functions using a nonlinear least squares method at the height of (c) 70.8 km and (d) 72.0 km. The circles denote the zonal wind components and the star marks denote the meridional components.
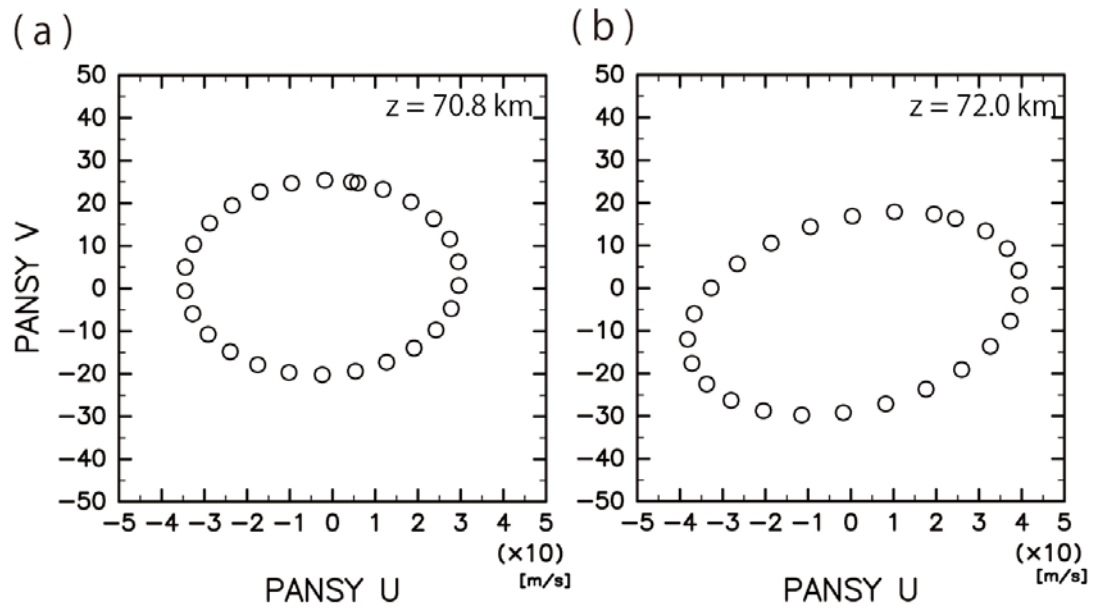
Figure 5 : A hodograph of the fitted horizontal wind components in the time region from 00 UTC 23 to 13 UTC 23 March at the height of (a) 70.8 km and (b) 72.0 km from the PANSY radar observation. Each mark is plotted at one hour interval.
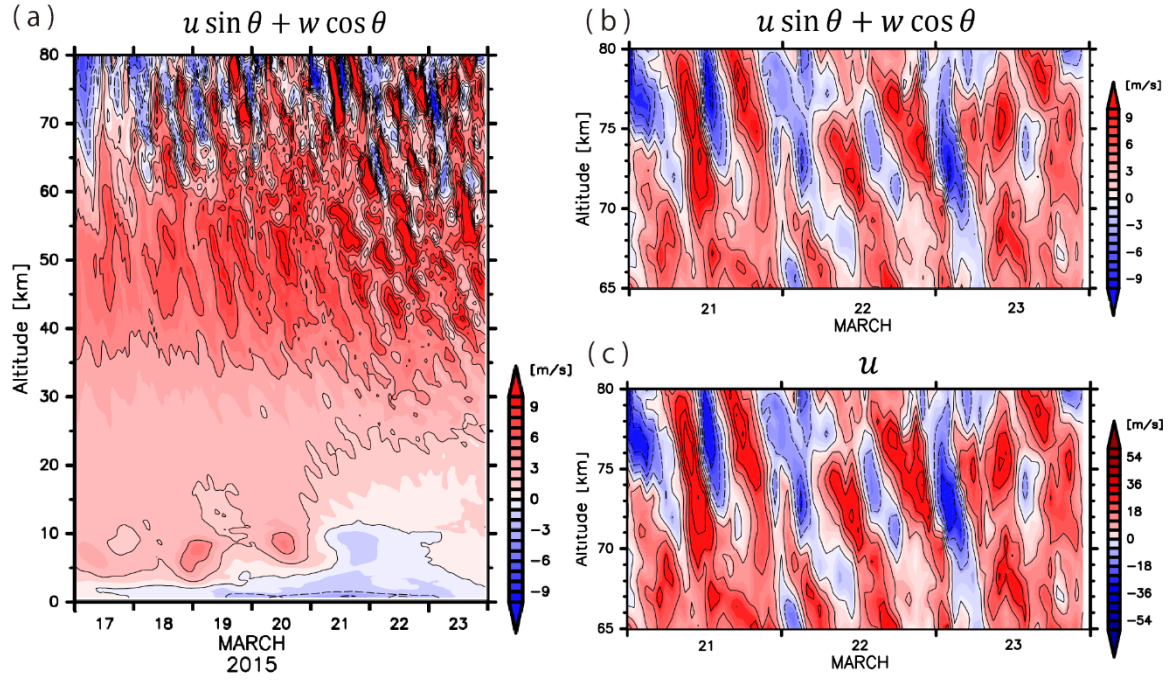
Figure 6: Time-altitude cross sections of (a) eastward line of sight velocity components simulated by NICAM at Syowa Station (contour interval 2 m s^{-1}) for the period from 17 March 2015 to 23 March 2015, (b) for the period from 21 March 2015 to 23 March 2015 (contour interval 3 m s^{-1}). (c) Zonal wind components in eastward line of sight velocity components for the period from 21 March 2015 to 23 March 2015 (contour interval 18 m s^{-1}).
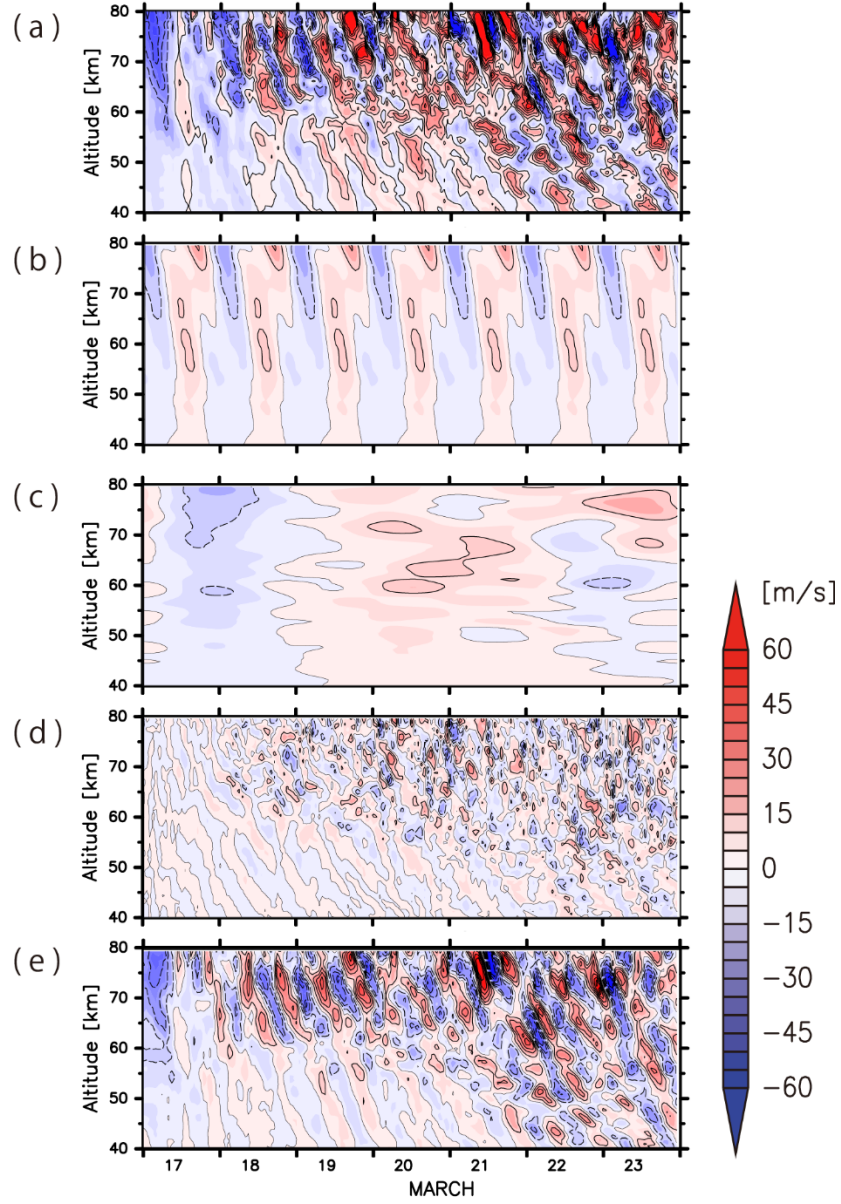
Figure 7: Time-altitude cross sections of (a) anomalies of the zonal wind components from the time-mean components, (b) the diurnal and semi-diurnal migrating tidal components, (c) the planetary wave components, (d) small-scale gravity waves and (e) the remaining components. The contour intervals are 10 m s⁻¹.
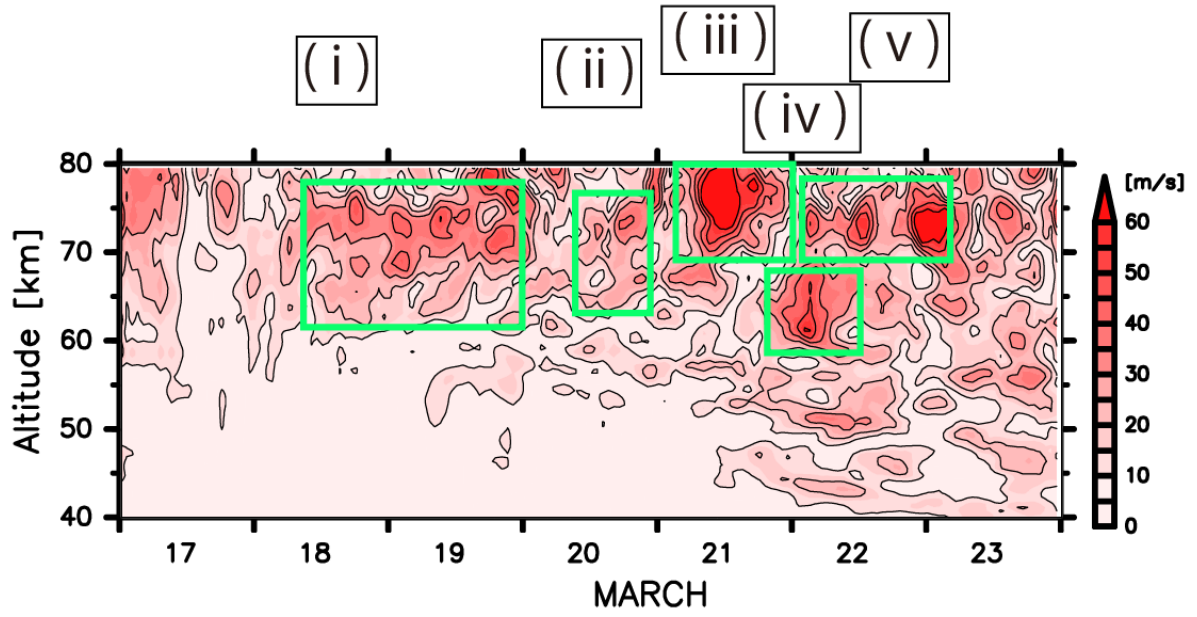
Figure 8: Time-altitude cross section of the envelope function of the zonal wind components of the large-scale gravity waves (contour interval 10 m $s^{-1}$) .The figure from (i) to (v) denote the labels of the wave packet examined in Section 4.
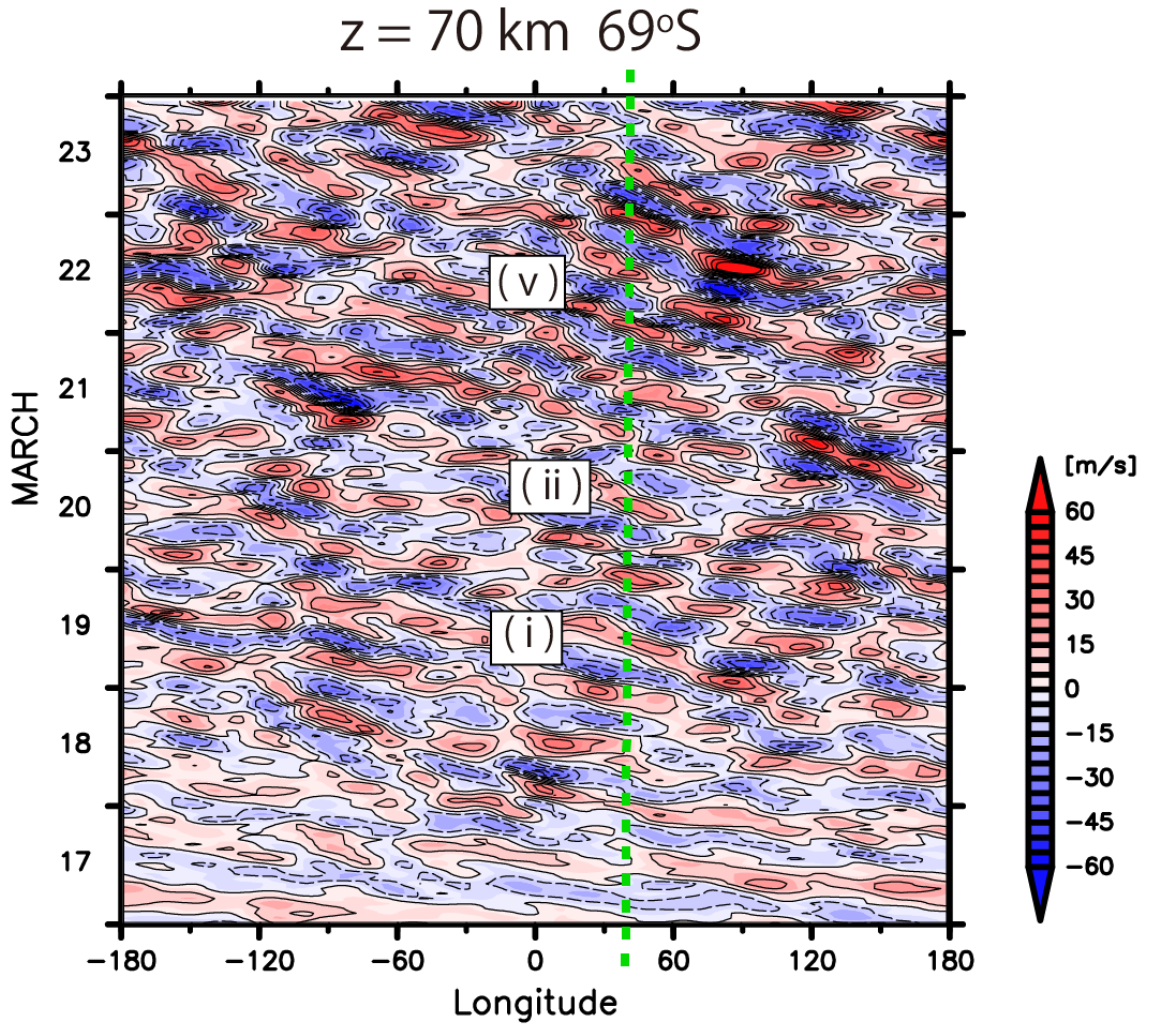
Figure 9: Hovmöller diagram of zonal wind components of the large-scale inertia-gravity waves at the height of 70 km at 69°S (contour interval 10 m s$^{-1}$). The figures (i), (ii) and (v) indicate the packets labeled in Fig.5.
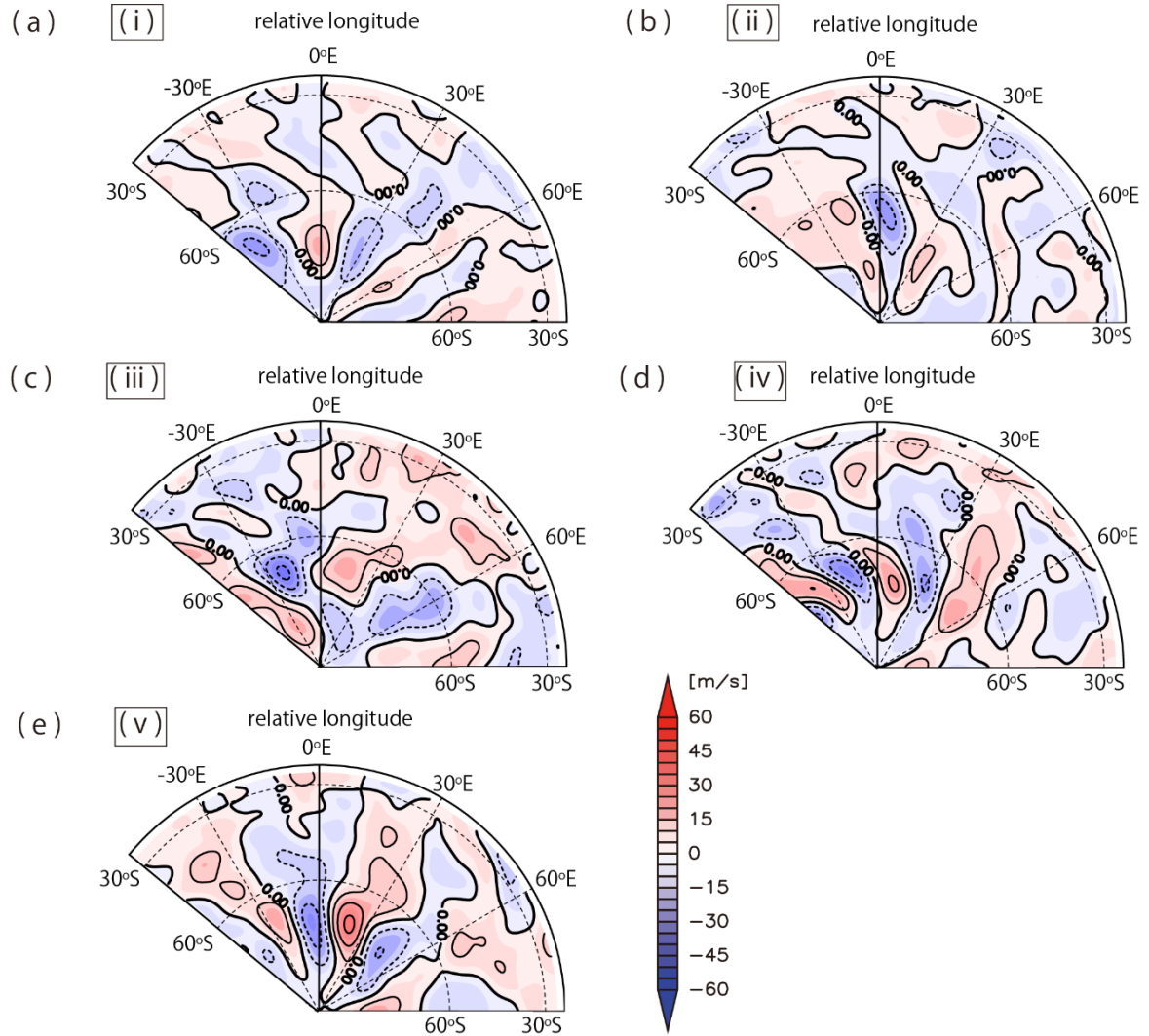
Figure 10: Composite maps of zonal wind components of the large-scale inertia-gravity waves. The height where the composites are taken is (a) 70 km, (b) 70 km, (c) 75 km, (d) 65 km, and (e) 72 km. The longitudinal location is depicted as the relative longitude from Syowa Station. The contour intervals are 10 m s^{-1}.
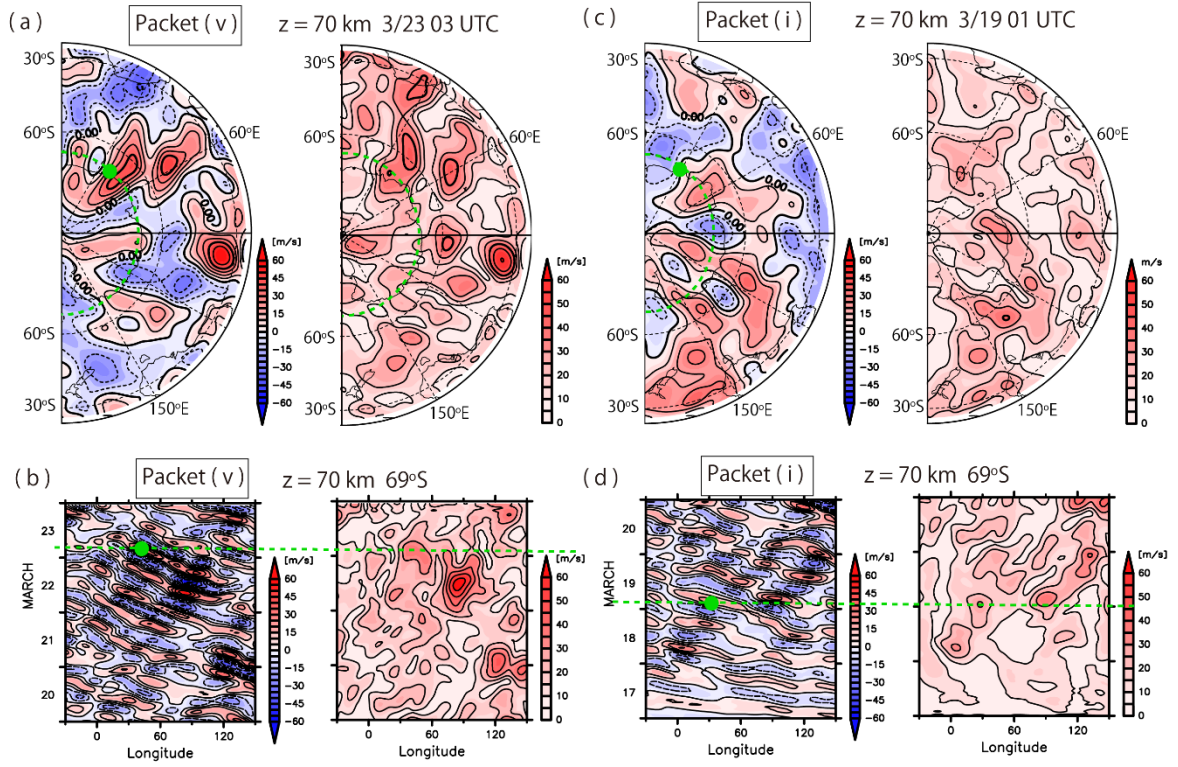
Figure 11: Snapshots of the zonal wind components and their envelope function of the large-scale inertia-gravity waves (a) at the height of 70 km at 03 UTC 23 March 2015, corresponding to the packet (v), and (c) at the height of 70 km at 01 UTC 19 March 2015, corresponding to the packet (i). Hovmöller diagrams of the zonal wind components and their envelope function of the large-scale inertia-gravity waves at the height of 70 km at 69°S for the period (b) from 20 to 23 March and (d) from 17 to 20 March. The green dashed curves in (a) and (c) denote the cross section taken in (b) and (d), and vice versa. The green circles are locations of traced wave packets determined by the method discussed in the text. The contour intervals are 10 m  $s^{-1}$.
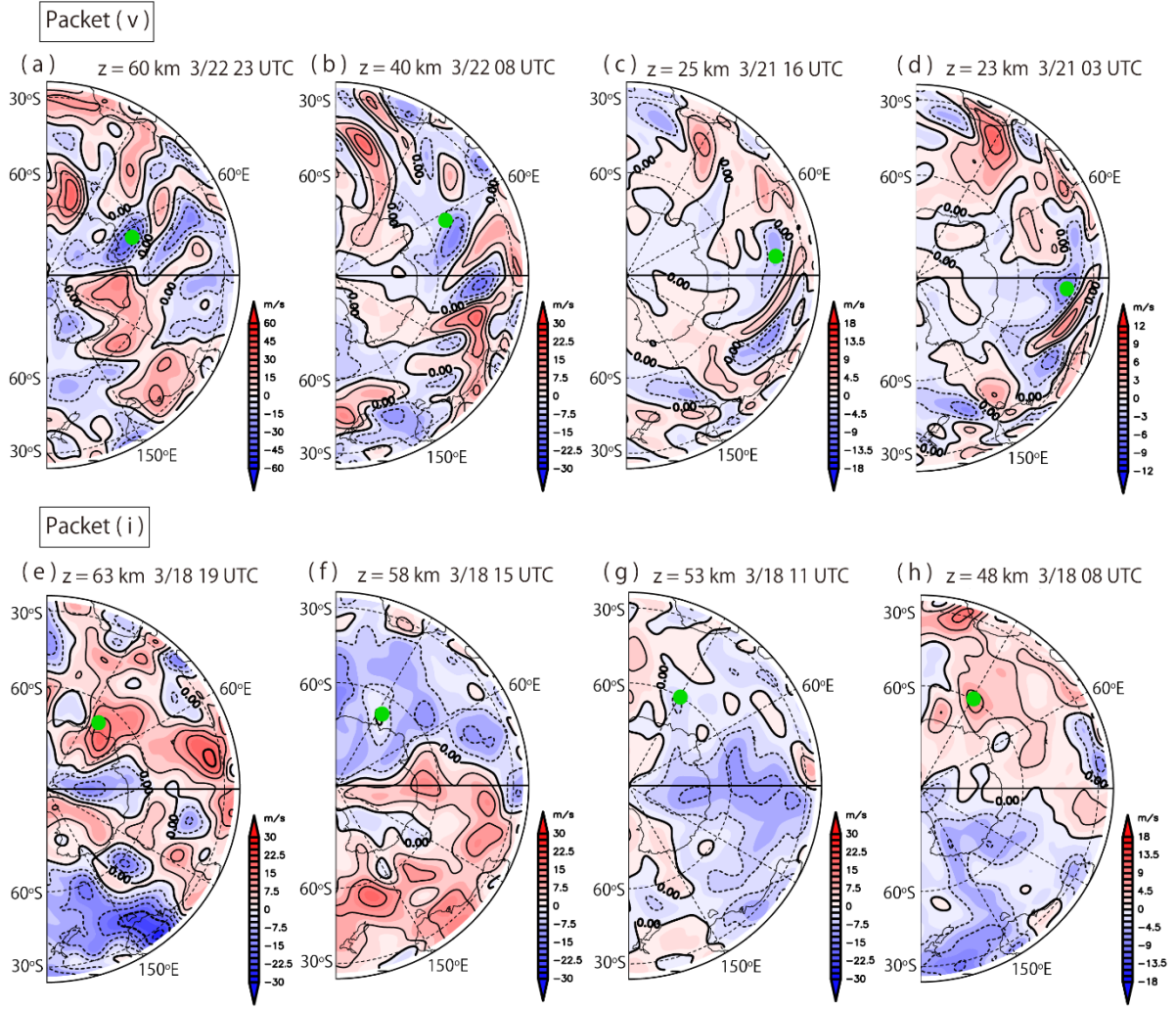
Figure 12: Snapshots of the zonal wind components of the large-scale inertia-gravity waves tracing the packet (v) (a) at the height of 60 km at 23 UTC 22 March (contour interval 10 m s$^{-1}$), (b) at the height of 40 km at 08 UTC 22 March (contour interval 5 m s$^{-1}$), (c) at the height of 25 km at 16 UTC 21 March (contour interval 3 m s$^{-1}$) and (d) at the height of 23 km at 03 UTC 21 March (contour interval 2 m s$^{-1}$). Snapshots for the packet (i) (e) at the height of 63 km at 23 UTC 22 March, (f) at the height of 58 km at 15 UTC 18 March, (g) at the height of 53 km at 11 UTC 18 March (contour interval 5 m s$^{-1}$), (d) at the height of 48 km at 08 UTC 18 March (contour interval 3 m s$^{-1}$). The green circles are locations of traced wave packets determined by the method discussed in the text.
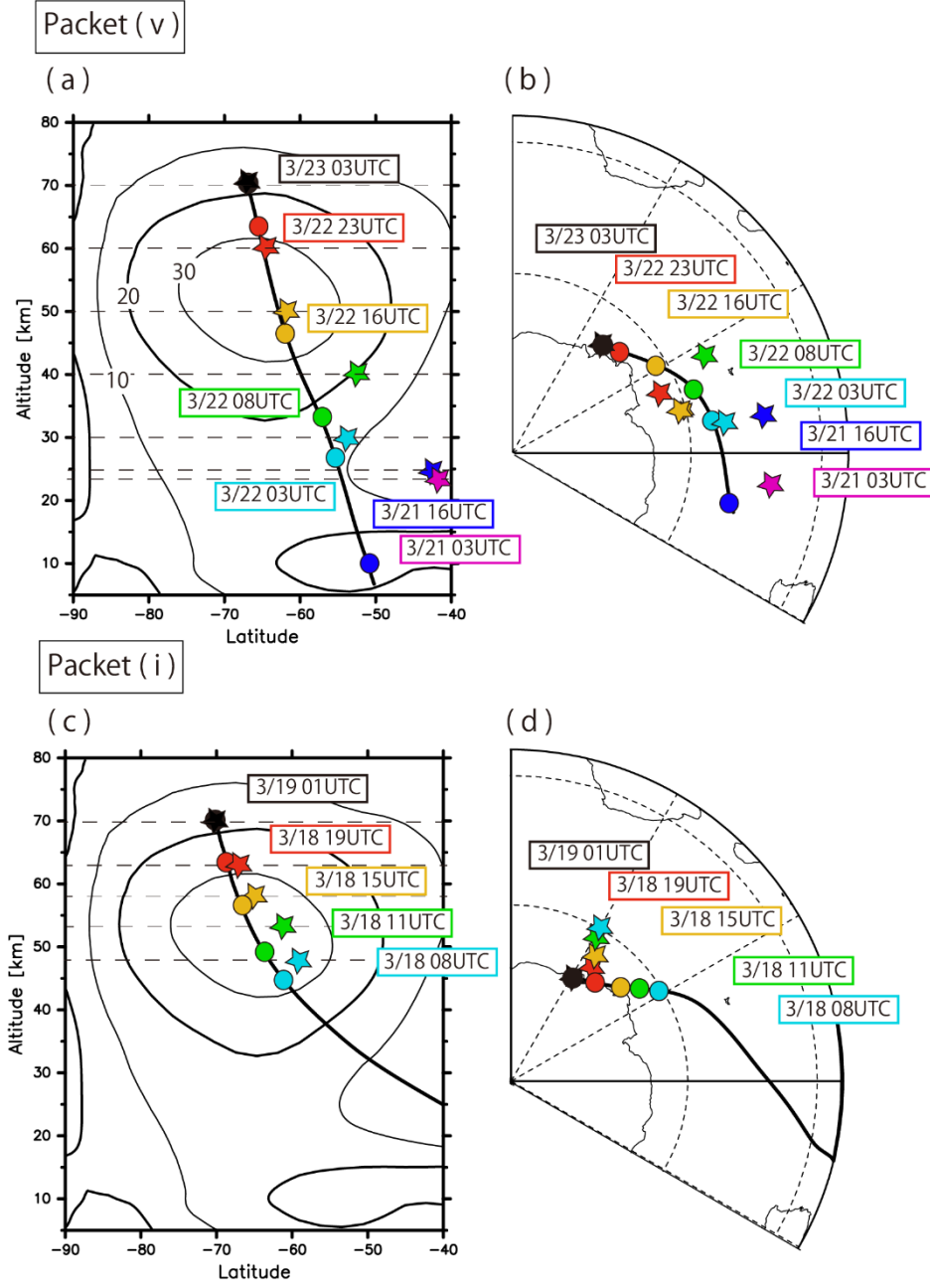
Figure 13: The ray path of (a, b) the packet (v) and (c, d) the packet (i) using the idealized ray tracing method (black thick line, colored circles) and the manual wave packet tracing method (colored star marks) in (a, c) the latitude-height cross section and (b, d) the horizontal map. The contours in (a, c) denotes background zonal wind components averaged in the zonal direction and for the period from 17 March to 23 March.
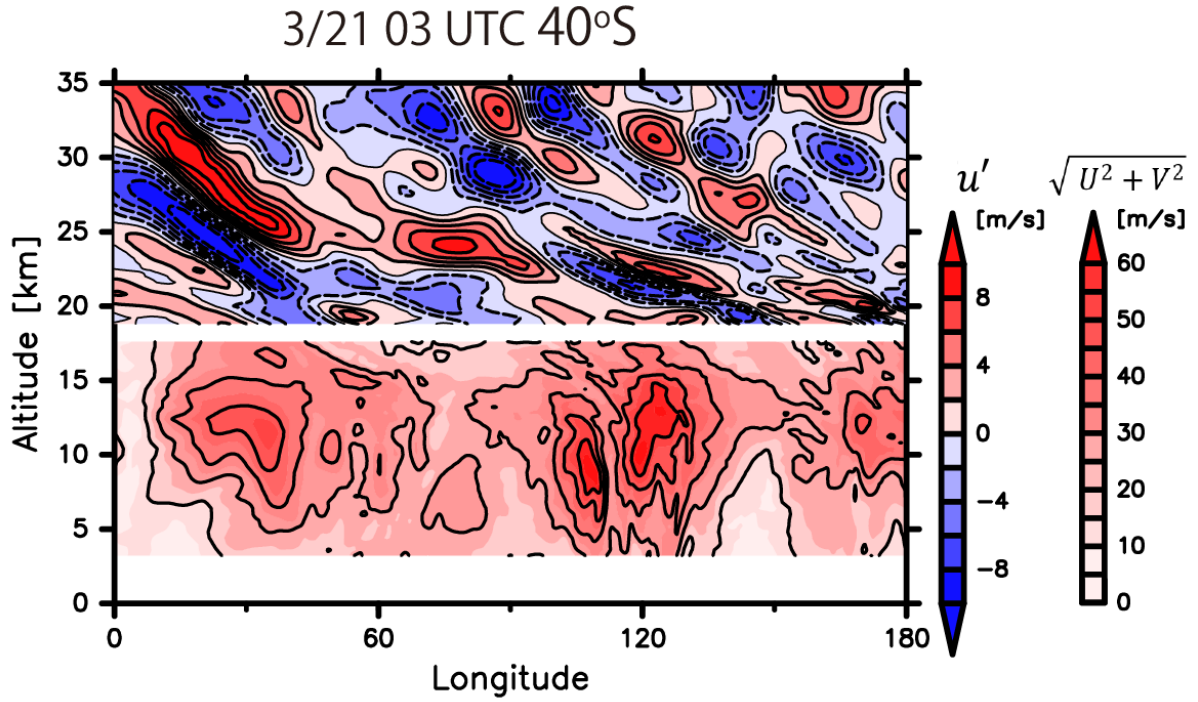
Figure 14: A snapshots of longitude-height cross sections of zonal wind components of the large-scale inertia-gravity waves (above the height of 19 km, the left color bar, contour interval 2 m s$^{-1}$) and the absolute values of the horizontal wind components (below the height of 18 km, the right color bar, contour interval 10 m s$^{-1}$) at 03 UTC 21 March at 40°S.
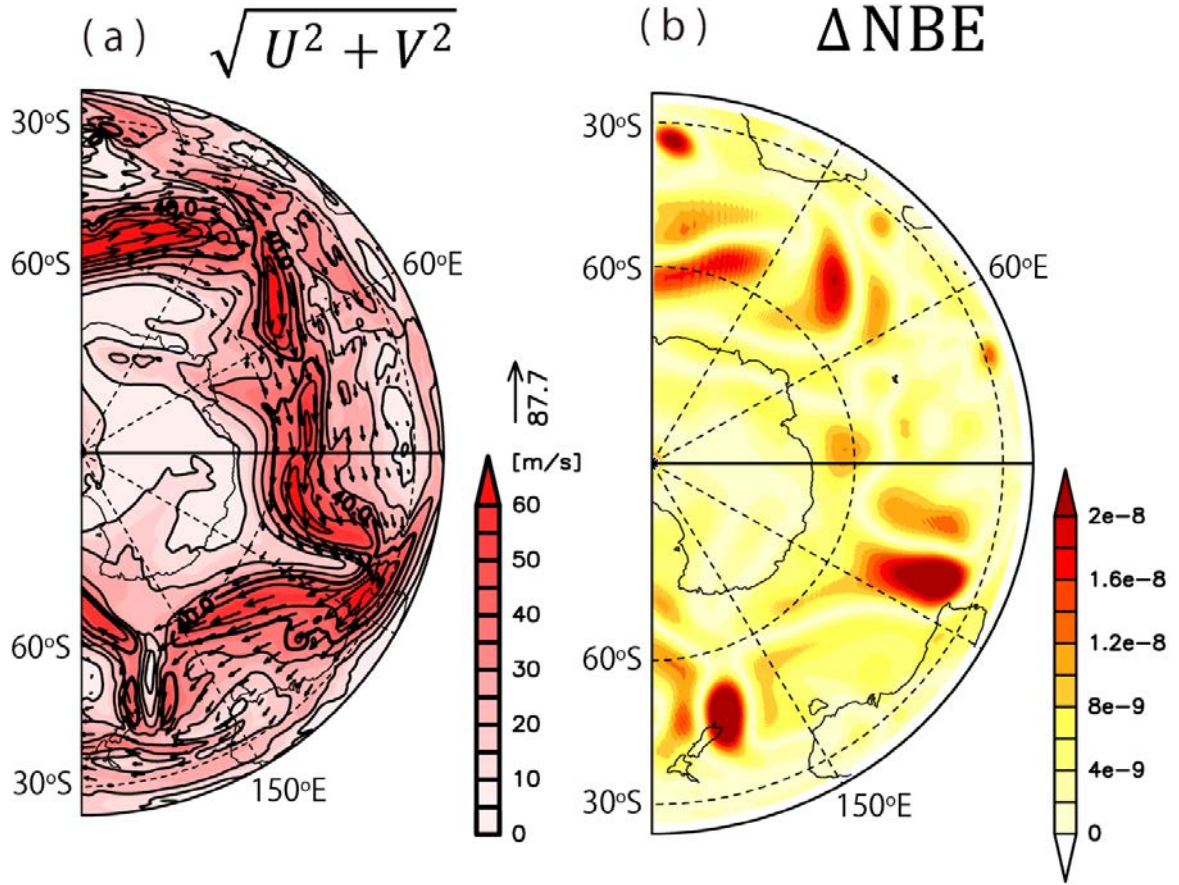
Figure 15: Snapshots of horizontal maps of (a) the absolute horizontal wind velocity and (b) the residual of the nonlinear balance equation ($\Delta NBE$) at the height of 10 km at 03 UTC 21 March 2015. The vectors in (a) denote the directions and the magnitude of the horizontal winds. The contour intervals in (a) are 10 m s$^{-1}$.
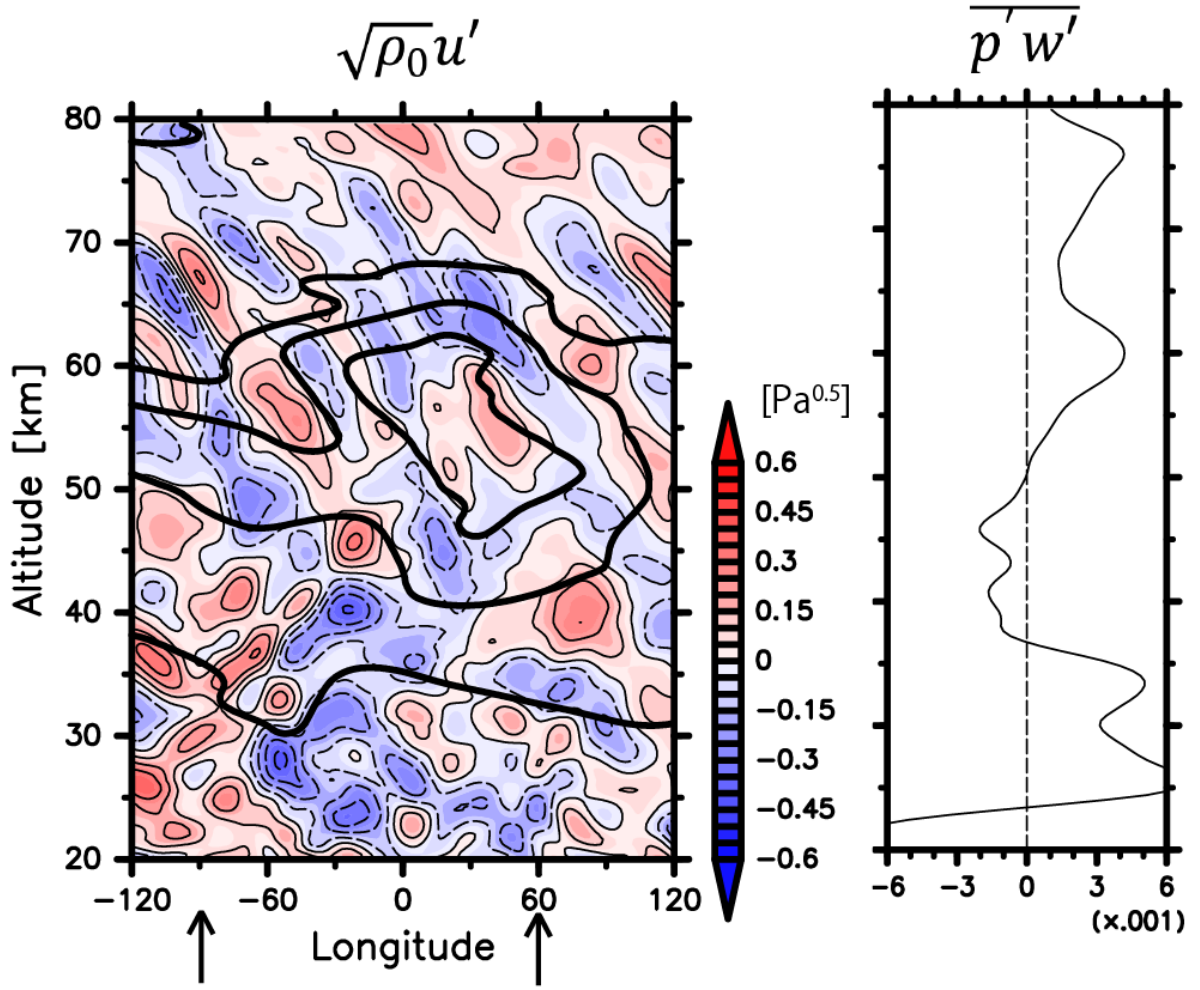
Figure 16: (a) A longitude-height cross section of zonal wind components of the large-scale inertia-gravity waves $\sqrt{\rho_0}u'$ at 65°S at 15 UTC 18 March (contour interval 0.1 Pa$^{0.5}$), and (b) a line plot of the energy flux $\overline{p'w'}$ averaged from the longitude of -90°E to the longitude of 60°E denoted by black arrows. The thick black contours show background zonal wind components extracted by a lowpass filter with a cutoff wavelength of 4000 km. The thick contours denote 20 m s$^{-1}$, 30 m s$^{-1}$ and 40 m s$^{-1}$, respectively.
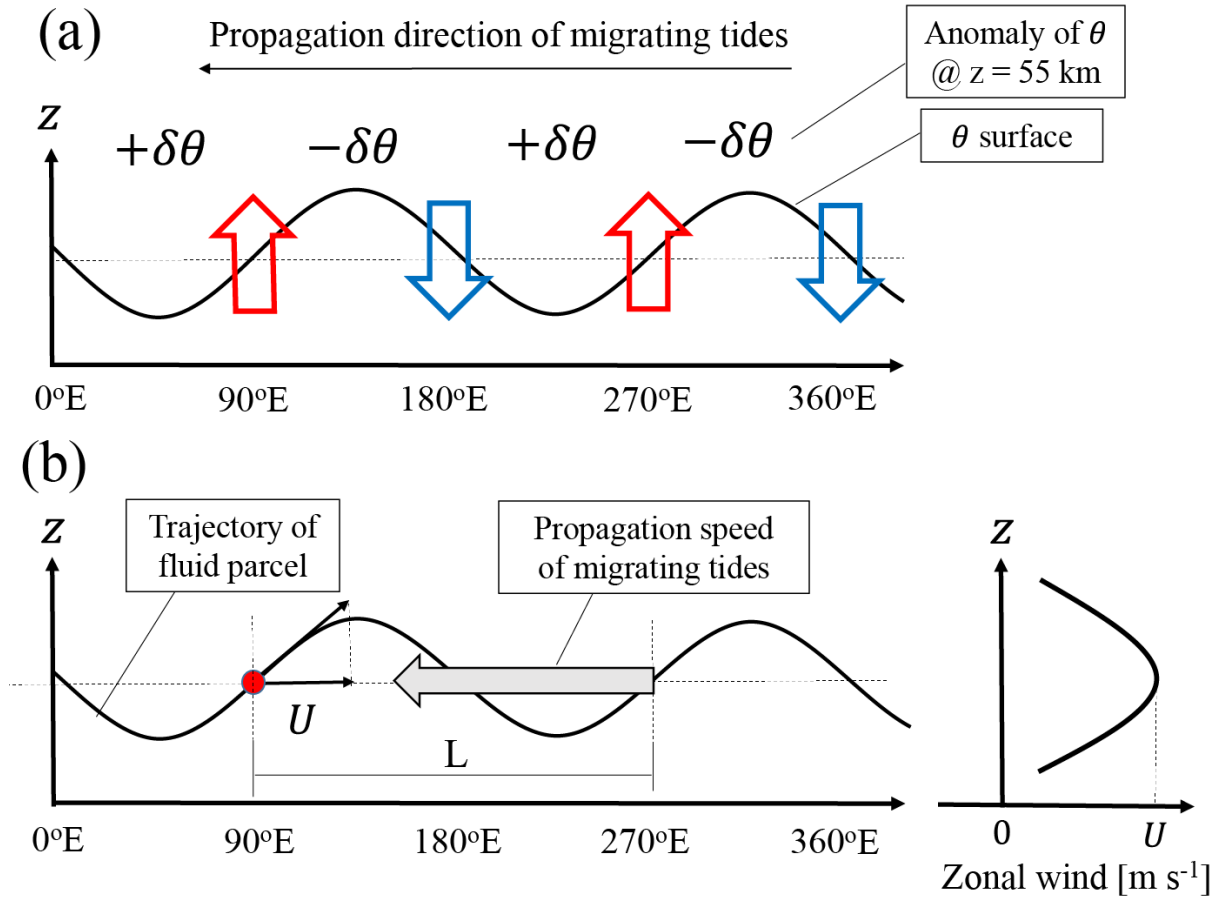
Figure 17: (a) a schematic figure of longitudinal locations of anomalies of $\theta$ ($\delta\theta$) from the zonal mean due to the semi-diurnal tide, and associated vertical wind couplets denoted by large arrows at a height of the core of the polar night jet. (b) A trajectory of fluid parcel on a $\theta$ surface at the height of polar night jet. The thin dashed arrow denotes a motion of the fluid parcel, and $U$ denotes the magnitude of the background zonal wind.
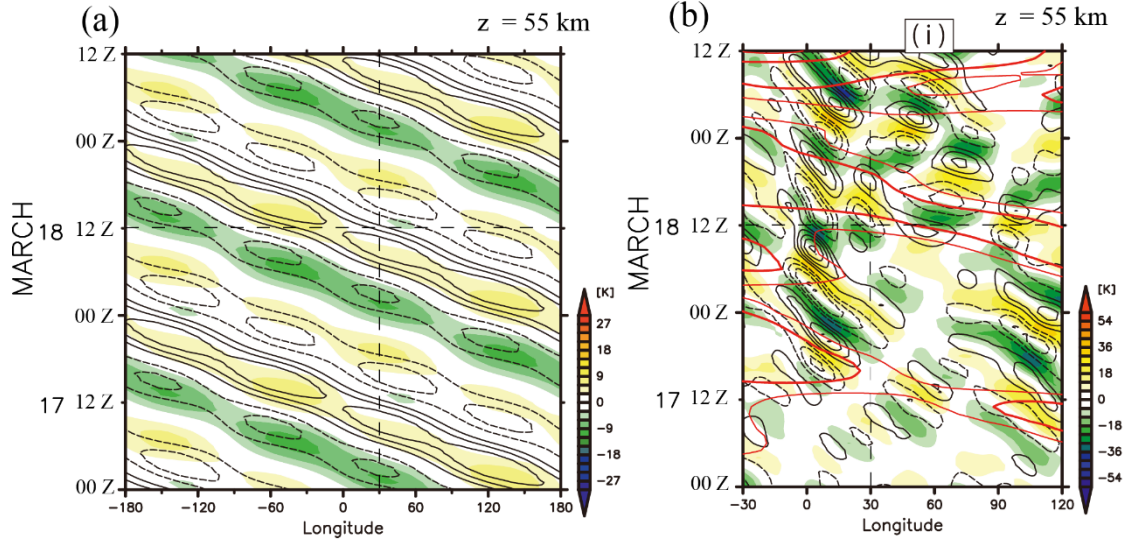
Figure 18: (a) A hovmöller diagram of potential temperature (shade) and the vertical wind components (contour) due to the diurnal and semi-diurnal migrating tides at the height of 55 km at 65°S. The contour interval is $0.5 \times 10^{-2}$ m s$^{-1}$. (b) A hovmöller diagram of potential temperature (shade) and the vertical wind components (black contour) of the large-scale inertia gravity waves, and the zonal wind component with $s = 1$ and $s = 2$ at the height of 55 km at 65°S. The black contour interval is $2.0 \times 10^{-2}$ m s$^{-1}$, the red thin contour denotes 30 m s$^{-1}$ and the red thick contour denotes 35 m s$^{-1}$.
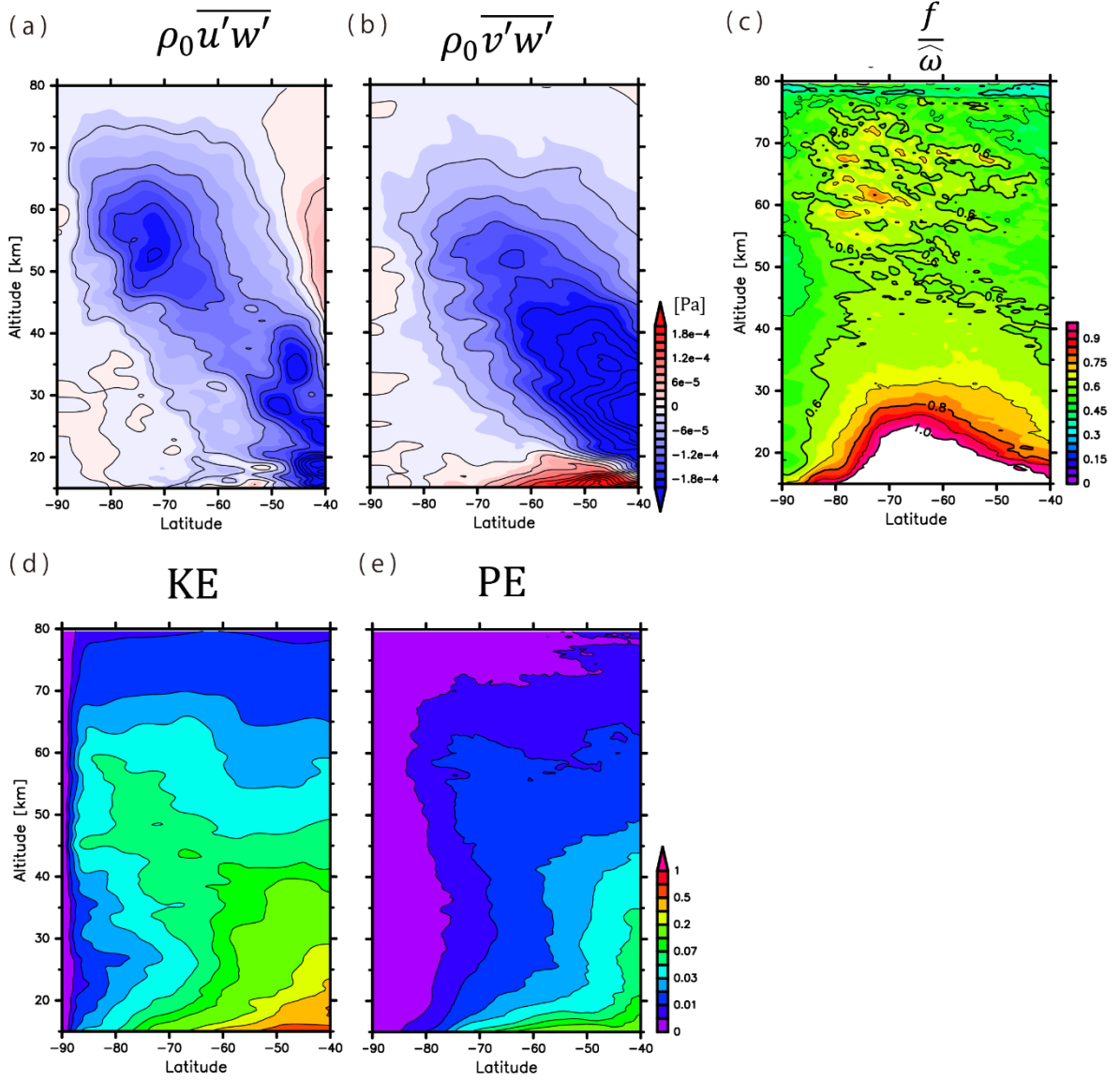
Figure 19: Latitude-height cross sections of (a) the vertical fluxes of zonal momentum $\rho_0\overline{u'w'}$, (b) the vertical fluxes of zonal momentum $\rho_0\overline{v'w'}$, (c) the ratio of the Coriolis parameter to the intrinsic frequency $f/\widehat{\omega}$, (d) the kinetic energies of the horizontal wind components and (e) the potential energies of the large-scale inertia-gravity waves, which are averaged in the zonal direction and for the period from 19 March to 21 March 2015. The contour interval is (a, b) $4.0 \times 10^{-5}$ [Pa] and (c) 0.1, respectively. It should be noted that the color bar and the contour interval in (d) and (e) are log-scaled.